J. Mech. Phys. Solids 206 (2026) 106375

Contents lists available at ScienceDirect

Journal of the Mechanics and Physics of Solids

journal homepage: www.elsevier.com/locate/jmps

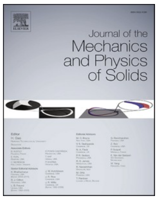

Non-proportional plastic deformation at the micron scale: Single crystal Cu cantilever beams subjected to orthogonal bending

Bin Zhang [a,1], Carl F.O. Dahlberg [b,1], Tim Fischer [b,c], J.W. Hutchinson [d,*], W.J. Meng [a,*]

[a] *Department of Mechanical and Industrial Engineering, Louisiana State University, Baton Rouge, LA 70803, USA*
[b] *Department of Engineering Mechanics, KTH Royal Institute of Technology, Stockholm, Sweden*
[c] *Institute of Materials Physics and Technology, Hamburg University of Technology, Hamburg, Germany*
[d] *School of Engineering and Applied Sciences, Harvard University, Cambridge, MA 02138, USA*

ARTICLE INFO

Keywords:
Strain gradient plasticity
Sequential cantilever orthogonal bending
Incremental and non-incremental SGP formulation

ABSTRACT

Experiments involving abrupt non-collinear changes in the direction of loading in the plastic range have been performed on micron-scale, single crystal Cu cantilever beams to provide the first data of its kind on non-proportional loading. The data is used to assess whether existing strain gradient plasticity (SGP) theories are capable of reproducing complex deformation histories representative of micron-scale metal forming processes, for which non-proportional loading is common. The data is also used to explore an issue that has arisen in efforts to develop SGP that is sufficiently accurate for engineering applications and yet not overly complex. Specifically, using a combination of experimentation and computation, the paper examines the differences in predictions made by two classes of theories presently in the mainstream, termed “incremental” and “non-incremental”, when non-proportional plastic loading occurs at the micron scale. Orthogonal bend experiments are performed on Cu single crystal cantilever beams with square cross-sections that are symmetrically oriented with respect to the vertical and horizonal bending axes. In Stage 1, the force applied to the end of the cantilever is vertical, producing bending in the vertical plane. Abruptly, in Stage 2, a horizontal force is applied with either the vertical force held constant (force control) or the vertical end-displacement of the beam held constant (displacement control). Three cantilever sizes, with widths of the square cross-section of 2, 5 and 20 microns, have been tested. The strength elevation for cantilever widths decreasing from 20 to 2 microns is about a factor of three as compared to what would be expected based on conventional plasticity theory. The incremental and non-incremental SGP theories both capture the full non-proportional loading history, including the size effect. However, they differ in their predictions of behavior in the early portion of Stage 2, due to the abrupt change in the loading path. This difference will be assessed with the aid of experimental test data.

1. Introduction

Fabrication of small-scale metal-based structures enables the construction of devices with diverse functionalities, including micro

---

* Corresponding authors.
E-mail addresses: jhutchin@fas.harvard.edu (J.W. Hutchinson), wmeng1@lsu.edu (W.J. Meng).

[1] B.Z. and C.D. contributed equally to this work.

https://doi.org/10.1016/j.jmps.2025.106375
Received 13 June 2025; Received in revised form 20 September 2025; Accepted 24 September 2025

gyroscopes (Verma et al., 2015), microchannel heat exchangers (Mei et al., 2008), radiative thermal management with controlled emissivity (Krishna and Lee, 2018), and microchannel bipolar plates for fuel cells (Wang et al., 2024). Processes for fabricating such metal structures often involve extensive plastic deformation, as in micromolding (Malek and Saile, 2004) and microforming (Geiger et al., 2001). When the characteristic dimension of plastic deformation is small, from a few hundred microns to a few microns, the plastic response of metals often shows an explicit dependence on size, exhibiting the so-called mechanical size effects. Size effects manifest in simple test configurations, e.g., indentation (Ma and Clarke, 1995), foil bending (Stolken and Evans, 1998), and wire torsion (Fleck et al., 1994), as well as in various metal microfabrication processes, e.g., micromolding (Chen et al., 2011) and microextrusion (Zhang et al., 2021).

The advent of various three-dimensional (3D) printing techniques has further opened the possibility of fabricating truly 3D metal-based lattice structures with designed geometries, or the so-called architected metallic cellular structures (du Plessis et al., 2022). While present laser-based 3D printing techniques, such as laser powder bed fusion (L-PBF) (Abd-Elaziem et al., 2022), limit the minimum size of printed features to several hundred microns, emerging 3D printing technologies such as electrochemical printing promise fully dense 3D metal structures with minimum feature size in the micron range (Schürch et al., 2023). As the characteristic size of the basic structural elements of metallic cellular structures decreases, their deformation can be expected to display increasingly prominent size effects.

To date, functional devices constructed from small-scale 3D metal structures mostly operate in the elastic regime, with little or no plastic deformation occurring to the structure/device during operation. Examples include micro gyroscopes (Verma et al., 2015) and microchannel heat exchangers (Mei et al., 2008). With metallic cellular structures being actively investigated for medical implants and lightweight automotive/aerospace structures, different failure modes of such structures are of increasing interest, including failure in compression/tension, bending, torsion, buckling, fatigue, and their various combinations (Benedetti et al., 2021). In terms of loading configurations, while loading in pure compression/tension, pure bending, or pure torsion is proportional, combined loading, e.g., compression/tension followed by bending or torsion involves non-proportional loading.

Currently observed mechanical size effects can be categorized into two classes. One class manifests when plastic deformation involves significant strain gradients, as in the demonstration by Fleck et al. in 1994 that torsional strengths of wires depend on their diameters (Fleck et al., 1994). Another class arises when the total deformed volume becomes small, without the presence of strain gradients, as in the demonstration by Uchic et al. in 2004 that the compression strength of cylindrical pillars depends on the pillar diameter as it decreases to ten microns and below (Uchic et al., 2004). In the latter case, the present consensus is that the observed size effects arise from the need for dislocation nucleation and the lack of dislocation interactions due to the small volume being tested (Greer and De Hosson, 2011). In the engineering applications cited above, plastic deformation occurs with significant strain gradients, as in metals being molded by a rigid punch (Chen et al., 2011, Zhang et al., 2021), metals being formed through rigid dies (Zhang et al., 2018), or metal trusses in lattice structures being buckled under compression load (Nielsen and Hutchinson, 2022). Some of these scenarios involve non-proportional loading. Developing plasticity models sufficiently accurate for engineering purposes that incorporate the effects of strain gradients and can predict outcomes of proportional and non-proportional loading is thus of significant engineering importance.

Much research effort has been devoted to developing plasticity theories which explicitly incorporate strain gradient effects, including those by Aifantis (Aifantis, 1984), Fleck and Hutchinson (Fleck and Hutchinson, 2001), Gudmundson (Gudmundson, 2004), Gurtin (Gurtin, 2004), Gurtin and Anand (Gurtin and Anand, 2009), and Fleck and Willis (Fleck and Willis, 2009). In formulating strain gradient plasticity (SGP) theories containing explicitly at least one material's length scale parameter, l, higher order stress quantities are involved as work conjugates to plastic strains and plastic strain gradients, as exemplified in the expression for internal work increment within a volume V:

$$\dot{W} = \int_V \left\{ \sigma_{ij}\dot{\varepsilon}^e_{ij} + \sum\nolimits_k \left(q^{(k)}\dot{\gamma}^k + q_s^{(k)}\gamma_s^{(k)} + q_r^{(k)}\dot{\gamma}_r^{(k)} \right) \right\} dV \tag{1.1}$$

where σ_{ij} is the symmetric Cauchy stress work conjugated to increments of elastic strain increment $\dot{\varepsilon}^e_{ij}$, $q^{(k)}$ are the shear stress quantities working through plastic slip increments,$\dot{\gamma}^{(k)}$, with $q_s^{(k)}$ and $q_r^{(k)}$ being, respectively, the micro stress quantities work conjugated to increments of the two in-plane slip gradients, $\dot{\gamma}_r^{(k)}$ and $\dot{\gamma}_s^{(k)}$, all of which are common to the structure of strain gradient plasticity (Muhlhaus and Aifantis, 1991, Fleck and Hutchinson, 1997, Gurtin and Anand, 2005), and which will be defined in more detail later in the paper.

Any formulation of SGP theories should satisfy the thermodynamic constraints of energy conservation and non-negativeness of entropy production (Coleman and Noll, 1963). As summarized by Fleck, Hutchinson, and Willis (FHW) (Fleck et al., 2014), at the present time, there are two main classes of SGP formulations satisfying the thermodynamic constraints. The main difference between the two classes of formulations lies in the constitutive formulation. The non-incremental theory takes *the stress quantities themselves*, $q^{(k)}$, $q_s^{(k)}$ and $q_r^{(k)}$, to depend on the increments of plastic slips and their gradients (Gudmundson, 2004, Gurtin, 2004, Gurtin and Anand, 2009). By contrast, the incremental theory takes *the increments of stress quantities*, $\dot{q}^{(k)}$, $\dot{q}_s^{(k)}$ and $\dot{q}_r^{(k)}$, to be proportional to the increments of plastic slips and their gradients (Hutchinson, 2012, Fleck et al., 2015). As described in detail in the FHW paper, this difference in SGP formulations leads to similar model outcomes in cases when plastic straining is proportional or nearly so, i.e., when

$$\left(\varepsilon^P_{ij}, \varepsilon^P_{ij,k} \right) = \lambda \left(\gamma^{(k)}, \gamma^{(k)}_{,s}, \gamma^{(k)}_{,r} \right) = \lambda \left(\gamma^{(k)0}, \gamma^{(k)0}_{,s}, \gamma^{(k)0}_{,r} \right) \tag{1.2}$$

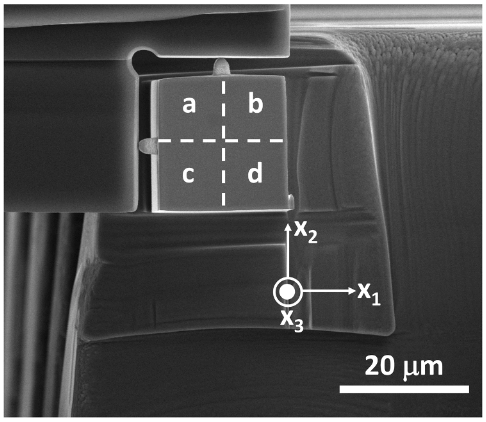

Fig. 1. Sequential orthogonal bending of one-end-attached cantilever beams with square cross-sections: an end view of one cantilever together with an actuator in contact with it. The Cartesian cantilever coordinates are indicated on the figure.

with λ increases monotonically and $\left(\gamma^{(k)0}, \gamma_{,s}^{(k)0}, \gamma_{,r}^{(k)0}\right)$ is independent of λ. However, different predictions arise when plastic straining is non-proportional which can occur when the loading direction changes abruptly giving rise to very different combinations of plastic slip. Briefly, in some applications with abrupt change in loading direction, the non-incremental formulation predicts unrealistic elastic or nearly elastic responses while the incremental theory predicts continued, but altered, plastic deformation. In the terminology of the FHW paper, an "elastic gap" occurs. In contrast, these unphysical elastic gaps are absent in the prediction from the incremental formulation (Fleck et al., 2014). It is noted that some recent works have examined the elastic gap problem in higher order gradient plasticity. Panteghini et al (Panteghini et al., 2019) proposed a distortion-gradient theory that avoids elastic gaps by construction, and Jebahi et al (Jebahi et al., 2020) introduced a generalized non-quadratic defect energy with uncoupled dissipation in a 2D crystal plasticity setting. Both Panteghini et al. and Jebahi et al. solved versions of the constrained simple shear problem to illustrate model behavior. More recently, Mukherjee & Banerjee (Mukherjee and Banerjee, 2024) have developed an isotropic elastic gap-free formulation and applied it to the micron scale proportional bending/torsion experiment of an L-beam.

To establish which SGP constitutive formulation more faithfully corresponds to actual non-proportional straining scenarios, it is necessary to test the outputs of the two different classes of SGP models against results of non-proportional loading experiments. Since strain gradient effects on plastic deformation typically manifest when the ratio of the material's length scale parameter l to the characteristic specimen dimension becomes significant and the magnitude of l typically ranges from 0.1 to 10 μm (Voyiadjis and Song, 2019), these experiments need to be executed at small length scales. To date, a number of small-scale mechanical loading experiments have been executed under proportional or nearly proportional conditions, including indentation (Ma and Clarke, 1995), foil bending (Stolken and Evans, 1998), cantilever bending (Motz et al., 2008), wire torsion (Fleck et al., 1994, Liu et al., 2012), and L-beam combined torsion and bending (Zhang et al., 2023). While experiments measuring materials' response under non-proportional loading conditions continue to be executed at the macroscale (Kuwabara et al., 2002, van Riel and van den Boogaard, 2007, Verma et al., 2011), to the best of our knowledge, no micro-/meso-scale non-proportional loading experiment involving an abrupt, non-collinear change in loading direction has been reported to date. It is noted that completely reversed deformation, such as reversed bending in the same plane or reversed torsion of a cylindrical wire specimen (Liu et al., 2013) constitutes a different kind of non-proportional loading example. In these problems, elastic unloading occurs initially on reversal and the two contending theories account for this correctly. It is also noted that there are important aspects that remain to be studied in the plastic deformation that occurs under reversed reloading in the micron scale range.

In this study, we conceptualize a small-scale experimental configuration involving non-proportional loading and illustrate the difference in predictions from non-incremental and incremental SGP formulations in this experimental scenario. We then realize such an experiment and compare the experimental results with outputs from a 3D SGP finite element analysis (FEA) simulation. In what follows, Section 2 describes this conceptualization. Section 3 describes the experimental procedures and the SGP modeling framework. Section 4 provides experimental results, modeling outcomes, and discussions. Section 5 gives a summary.

2. Conceptualization

We conceptualized an experiment involving non-proportional plastic loading of single crystal cantilever beams with square cross sections and cross-sectional width w. As illustrated in Fig. 1 and described in detail in the next section, one-end-attached, micron-sized cantilevers are first bent into the plastic range in the vertical plane by applying a vertical bending load in the $-x_2$ direction (Stage 1). Then, with either the vertical force or the vertical end-displacement held constant, a horizontal bending load in the $+x_1$ direction is applied, producing horizontal displacements and further changes in the vertical plane (Stage 2). Dividing the cantilever cross section into quadrants a, b, c, d, as shown in Fig. 1, the dominant stress experienced in Stage 1 in quadrants a and b is tension while that experienced by quadrants c and d is compression. The strain gradients in Stage 1 are in the vertical direction (x_2). By contrast, Stage 2

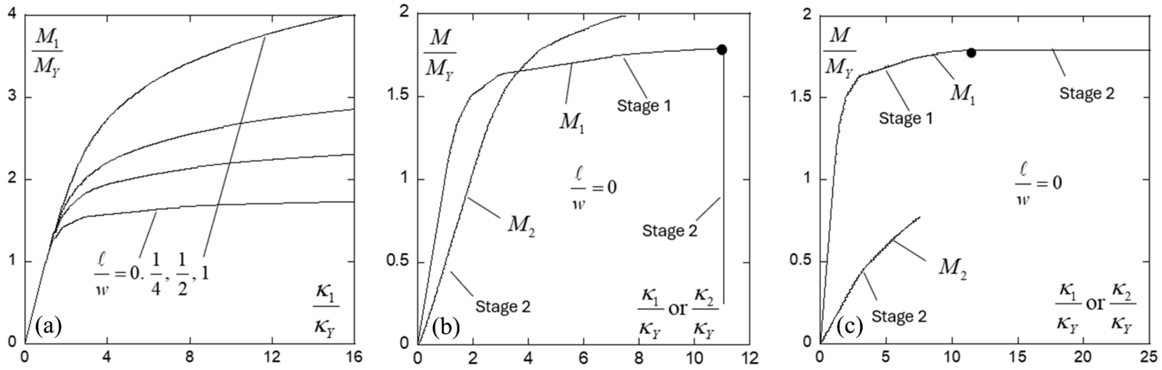

Fig. 2. Pure bending of an FCC Cu single crystal cantilever beam with square cross-section of width w, as predicted by the incremental SGP theory: The crystal axes are aligned with the Cartesian cantilever axes (x_i shown in Fig. 1), with x_3 parallel to the beam long axis. (a) displays the influence of the material length parameter in pure bending about x_1 (or x_2). The results in (b) and (c) for two-stage orthogonal pure bending are computed with no gradient effects ($l/w = 0$ with $N = 0.1$ and $h/\tau_Y^o = 0.1$) and, thus, are those for classical single crystal plasticity. The moment-curvature responses are presented for orthogonal bending with κ_1 held constant in Stage 2 in (b) and with M_1 held constant in (c). Solid dots mark the transition from Stage1 to Stage 2.

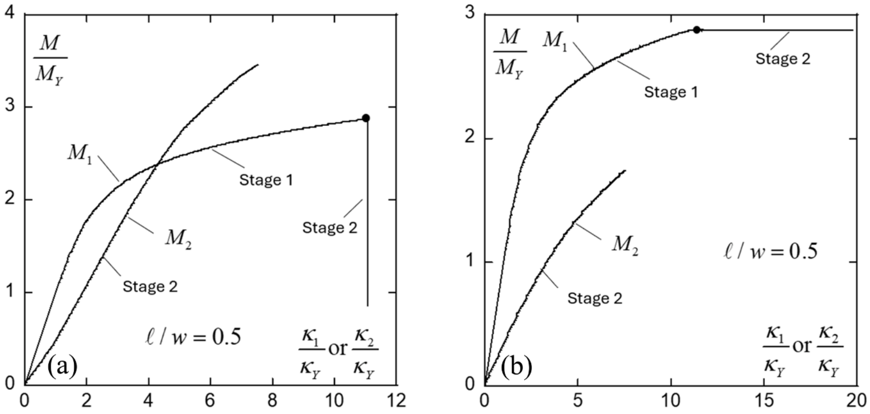

Fig. 3. Two-stage orthogonal pure bending of an FCC Cu single crystal beam with square cross-section of width w, as predicted by the incremental SGP theory with gradient effects ($l/w = 0.5$ with $N = 0.1$ and $h/\tau_Y^o = 0.1$). The crystal axes are aligned with the Cartesian cantilever axes (x_i shown in Fig. 1), with x_3 parallel to the beam long axis. The moment-curvature responses are presented for orthogonal bending with κ_1 held constant in Stage 2 in (a) and with M_1 held constant in Stage 2 in (b). Solid dots mark the transition from Stage 1 to Stage 2.

bending puts quadrants a and c in tension and quadrants b and d in compression. Moreover, the dominant strain gradient changes in Stage 2 switch to being in the horizontal direction (x_1). As the cantilever is subjected to Stage 1 and Stage 2 bending in sequence, quadrants b and c experience, respectively, tension followed by compression and compression followed by tension, and at the transition between stages, there is an abrupt addition of a strain gradient component in the horizontal direction in all the quadrants. Thus, this orthogonal bending represents a clear non-proportional loading scenario. The most relevant aspect to the difference between the incremental and non-incremental SGP theories is the abrupt switch in the direction of the strain gradients. For crystallographic simplicity, we chose to fabricate the cantilever out of FCC single crystals.

To aid the conceptualization, we include in this section orthogonal-bend predictions for the analogous, but simpler, case of pure bending of cantilever beams with square cross-sections of width w, first in the vertical plane (x_2–x_3) and then in the horizontal plane (x_1–x_3). Pure bending refers to bending such that the curvature, κ, changes are independent of the x_3 coordinate aligned with the cantilever centerline. Predictions from the incremental and non-incremental SGP theories for the pure double-bend scenario will highlight the differences between them in the clearest manner. Details of the two constitutive models and the computational methods used to generate results will be presented later in the paper.

Figs. 2 and 3 present behavior in dimensionless form computed using the incremental single crystal SGP model. The FCC crystal axes are aligned with the Cartesian cantilever axes (x_i shown in Fig. 1), with x_3 parallel to the beam centroid such that the combination of specimen geometry and crystal symmetry ensures that pure bending about the x_1 and x_2 axes are identical. The cubic elastic moduli are taken to be those of Cu, given later in the paper. The size effect due to strain gradients is displayed in Fig. 2(a) for monotonic bending about either of the two axes. The limit $l/w = 0$ is classical single crystal plasticity with no gradient effects. The elevation in bending strength due to plastic strain gradients is roughly a factor of 3 for $l/w = 1$ compared to the classical limit. While no effort has

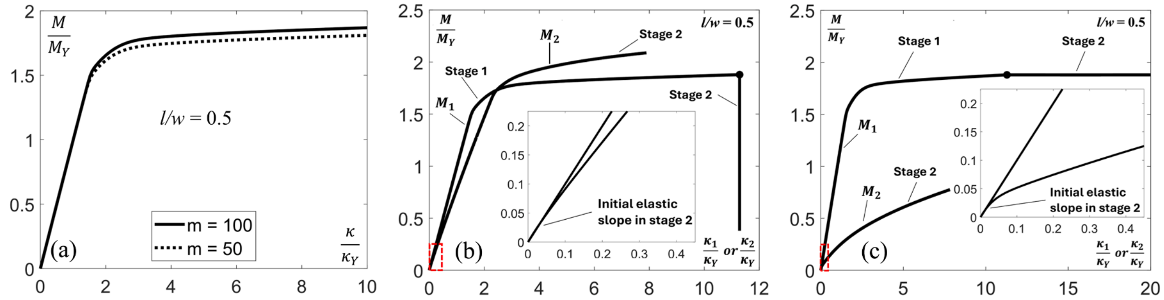

Fig. 4. Predictions for orthogonal pure bending based on the non-incremental SGP theory, with $l/w = 0.5$. (a) Illustration of the dependence of Stage 1 behavior on the strain rate parameter m. The value $m = 100$ is very close to the rate-independent limit, and it will be used in all the present simulations for this theory. (b) Moment-curvature behavior for the case with κ_1 held constant in Stage 2. (c) Moment-curvature behavior for the case with M_1 held constant in Stage 2. The inserts in (b) and (c) show expanded views of the initial portions of the moment-curvature relationships (within the red dashed boxes) and demonstrate that the initial relation of M_2 and κ_2 immediately after the transition to Stage 2 is governed by the elastic bending stiffness, but only for a short period.

been made to fit the parameters of the constitutive model in the pure bending simulations to the plastic slip behavior of Cu, as will be done later for the cantilever simulations, the smallest Cu cantilever specimens tested have l/w on the order of unity with strength elevation similar to that shown in Fig. 2. In Fig. 2, the responses with no gradient effects ($\ell/w = 0$) computed with constant curvature κ_1 in Stage 2 are shown in Fig. 2(b) and with constant moment M_1 in Stage 2 in Fig. 2(c). In this figure, and in Figs. 3 and 4, the normalizing factors (M_Y, κ_Y) are the moment and curvature values at initial yield in pure bending about either axis for the case with aligned crystal axes:$M_Y = 2\sqrt{2/3}\,\tau_Y^0 w^3$ and $\kappa_Y = \sqrt{3/2}\tau_Y^0/L_4 w$, with τ_Y^0 as the initial yield stress of the slip systems and L_4 as the elastic modulus governing uniaxial stressing along the beam long axis x_3.

The corresponding behavior in orthogonal pure bending in the presence of strain gradient effects according to the incremental theory is seen in Fig. 3, with $\ell/w = 0.5$. The behavior of the beams with $\ell/w = 0.5$ is similar to that with no gradient effects ($\ell/w = 0$), except for the significant elevation in the stress level. Note for further discussion that plasticity significantly reduces the incremental bending stiffness relating M_2 to $\kappa_2$below the elastic stiffness for both the classical theory shown in Fig. 2 and the incremental SGP theory shown in Fig. 3.

Results of orthogonal pure bending simulations based on the non-incremental single crystal SGP theory are presented in Fig. 4, with $\ell/w = 0.5$. Fig. 4(a) is included to give some indication of the role of the strain rate parameter m introduced in the model to facilitate the numerical implementation of this formulation. The rate-independent limit is $m \rightarrow \infty$. The simulations reported in this paper for the non-incremental theory use $m = 100$, which deliver results close to this limit. The hardening law employed in the non-incremental model is not the same as that employed in the incremental model simulations, and this difference is evident when the two sets of simulations are compared. Otherwise, the two sets of simulations are similar in most of the details. As shown most clearly in the insets of Figs. 4(b) and 4(c), there is a strict elastic gap immediately following the transition to Stage 2, but it is quite small. For the case in which κ_1 is held constant in Stage 2, The slope of M_2 versus κ_2 is approximately 1/2 the elastic slope for the incremental prediction in the range $0 < \kappa_2/\kappa_Y < 2$, while that slope is greater than 3/4 according to the non-incremental theory in that same range. By physical reasoning, a value of close to 1/2 should be expected. After the transition to Stage 2, two of the four quadrants in Fig. 1 unload elastically, and it is the incremental stiffness of the elastic regions that dominate the contributions to the incremental bending stiffness. For the case in which M_1 is held constant in Stage 2, the range of κ_2 in which there is a significant difference between the incremental and non-increments predictions is smaller.

In summary, the cantilever orthogonal-bend experiment is a well-chosen test to assess non-proportional loading effects at the micron scale. Within the context of conventional plasticity with no strain gradient dependence, the stress state in the beam is approximately uniaxial with σ_{33} as the primary stress component. Non-proportionality in this context is associated with plastic loading/elastic unloading behavior, which is well understood. In the context of strain gradient plasticity for micron scale bending, the dominant aspect of the non-proportionality is the switch in the gradients of plastic strain from being primarily normal to x_1 in Stage 1 to being normal to x_2 in Stage 2. This gradient switch is the essence of what gives rise to the difference in the predictions of the incremental and non-incremental SGP theories. The orthogonal pure bending simulations reveal that some difference between the two SGP theories being considered should be expected immediately following the transition from Stage 1 to Stage 2, but, depending on the application, the difference may not be important because the two competing predictions become similar past the transition.

3. Experimental procedure and simulation framework

3.1. Experimental procedures

Sequential orthogonal bending of Cu single crystal cantilevers was carried out. Commercial <100> oriented Cu single crystals, with dimensions of 5 mm × 5 mm × 1 mm (MTI Corporation), were used to fabricate one-end-attached cantilever beam specimens with width w, thickness t, and length l. Square cantilever beam specimens were fabricated with the same dimensional ratio of $l = 3w = 3t$

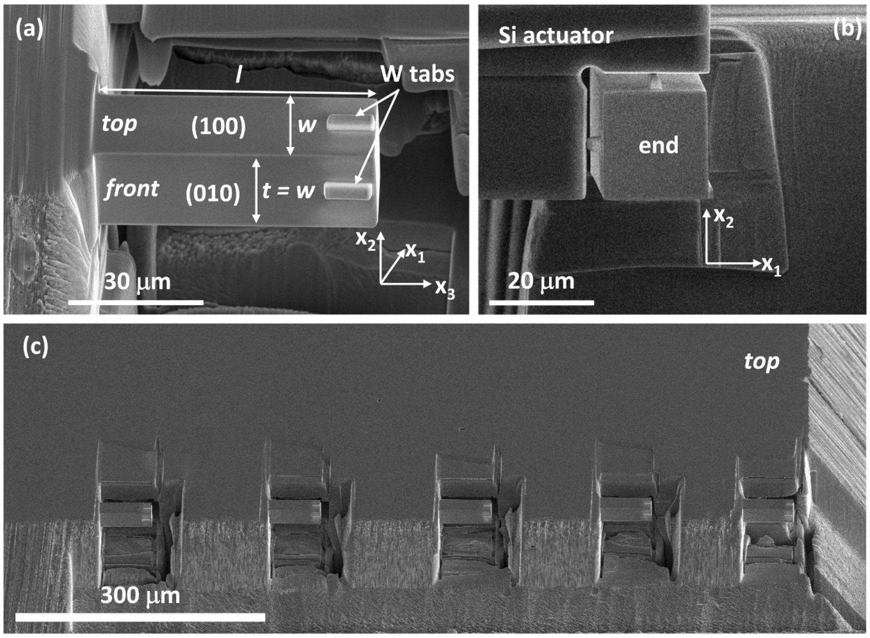

Fig. 5. Sequential orthogonal bending of one-end-attached Cu <100> square cantilevers: (a) one as-fabricated cantilever with dimensions of 20 μm × 20 μm × 60 μm; (b) one still-frame in a video taken during an orthogonal bending of one 20 μm cantilever; (c) a low magnification image of an array of as-fabricated 20 μm Cu <100> cantilevers. The dimensions of the W tabs are 2 μm × 2 μm × 10 μm. Bending was conducted sequentially, first in $-x_2$ direction then in $+x_1$ direction.

using a Xe$^+$ plasma focused ion beam/scanning electron microscope instrument (PFIB/SEM, ThermoFisher Helios G5 CXe) with energy dispersive spectroscopy (EDS, Oxford Instruments Ultim®Max) and electron backscatter diffraction (EBSD, Oxford Instruments Symmetry®) attachments and a MultiChem$^{\text{TM}}$ gas injection system for ion beam catalyzed, site-selective deposition of W. Three series of square cantilevers with $w = 20$ μm, 5 μm, and 2 μm were fabricated. A Xe$^+$ ion beam of 30 keV and 0.3 nA was used in the finish machining step for all cantilever beam surfaces. The same PFIB/SEM instrument was used for surface imaging by SEM and crystal orientation determination by EBSD. The single crystal nature of the fabricated Cu <100> cantilever specimens is demonstrated in an EBSD pole figure dataset obtained from the top surface of a typical Cu cantilever specimen, shown in Section S1 of the Supplemental Information (SI) document.

An instrumented nanomechanical testing system (FemtoTools NMT04) with custom-developed control capabilities, allowing independent and programmable actuation in two orthogonal directions ($-x_2$ and $+ x_1$), was used to carry out cantilever orthogonal bending tests in-situ a FEI Quanta3D FEG Ga$^+$ FIB/SEM instrument. The tip region of a Si actuator was shaped through Xe$^+$ PFIB milling to allow engagement with the square Cu cantilevers and loading in two orthogonal directions. Prior to actual experimentation, the loading system stiffness values in x_2 and x_1 directions were measured by contacting the Si actuator to the Cu single crystal bulk, applying sufficiently small loads such that no indentation occurs, and measuring the registered load – displacement response. This measured compliance was subtracted from the actual cantilever loading data to remove the system stiffness contribution. Further details on system stiffness measurement are reported in Section S2 of the SI document.

Fig. 5 illustrates the single crystal Cu <100> cantilever beam specimen and the sequential cantilever orthogonal bending experiment. Fig. 5(a) shows one as-fabricated cantilever with width $w = 20$ μm, thickness $t = 20$ μm, and length $l = 60$ μm. The normal to the cantilever top and front surfaces are parallel to the [100] and [010] directions of Cu, respectively. The cantilever long axis is parallel to the Cu [001] direction. That is, the FCC Cu crystal axes are aligned with the (x_i) axes of the cantilever beam specimen (see Fig. 1). Two W tabs, with dimensions of 2 μm × 2 μm × 10 μm, were site-selectively deposited onto the end of cantilever beam top and front surfaces. The ratio of the W tab length to the cantilever length is 1:6. This ratio was maintained for all cantilever sizes. Fig. 5(b) shows one still-frame in a video taken during orthogonal bending of one 20 μm square Cu <100> cantilever. The entire video is presented in Section S3 of the SI document and gives a more intuitive impression of the experiment, including the fact that the presence of the W tabs does not cause localized plastic deformation of Cu. More details are presented in Section S3 of the SI document. End loads were applied sequentially, first in $-x_2$ direction then in $+x_1$ direction. The tip region of the Si actuator, as seen in Fig. 5(b), was shaped by PFIB milling to present a square corner, with which engagement was made with W tabs deposited onto the cantilever top and front surfaces before bending loads were applied. The thickness of the Si square corner region was ~8 μm, ensuring that the initial contact between the Si actuator and the cantilever was entirely confined to the W tabs. A separate Si actuator with the same square corner shape but a smaller thickness of ~1 μm was fabricated and used for orthogonal bending of 5 μm and 2 μm Cu <100> cantilevers. The W tabs reduced the area of contact between the cantilever and the Si actuator, without which stick/slip occurred between the cantilever and the Si actuator, causing periodic serration in measured force – displacement curves. Further details are shown in Section S4 of the

SI document. Contacts between the Si actuator and the W tabs on the cantilever top and front surfaces leaves distinguishable marks, from which the load length l_L (distance from the cantilever attachment to the load point) is measured from post-testing micrographs. Fig. 5(c) shows a low magnification image of an array of as-fabricated 20 μm Cu <100> cantilevers. Repeat tests were generated through loadings on separate cantilevers.

Two separate experiment data groups were collected. For the first data group, cantilever bending in both x_1 direction and x_2 direction was executed under force-control. For the second group, bending in x_2 direction was executed under displacement-control while bending in the $x_1$direction was executed under force-control. A raw dataset consists of a complete time history of loading force and actuator displacement in both x_1 and x_2 directions. The loading rate and displacement rate during tests were kept below 50 μN/s and 40 nm/s for all tests, adjusted to keep an effective strain rate to below 2 × 10^{-3}/sec. A table cataloging the cantilever orthogonal bending experiments is provided in Section S5 of the SI document.

3.2. Two strain gradient plasticity theories for single crystals

We have strived to use the simplest meaningful versions of single crystal SGP formulation consistent with small strains and rotations. In this section, the incremental and non-incremental versions of the theory are defined. As shown later, the two versions coincide when the loading is proportional if the same physical properties are used for each. Rate-independent versions will be presented in this section, but an extension to a rate-dependent formulation is given in Section S6 of the SI document, which is used for numerical computations following the non-incremental formulation. Details directly related to the calculations for the orthogonal bend problems are also given in Section S6 of the SI document.

The elastic moduli of the single crystal are denoted by L_{ijkl}. With plastic strains denoted by ε^P_{ij}, $\sigma_{ij} = L_{ijkl}\varepsilon^e_{kl}$ where the elastic strain is $\varepsilon^e_{ij} = \varepsilon_{ij} - \varepsilon^P_{ij}$. The crystal has M slip systems with the slip on the k^{th} system denoted by $\gamma^{(k)}$. The unit normal to the slip plane is $m^{(k)}_i$ and the unit vector in the slip direction is $s^{(k)}_i$. The plastic strain arising from slip contributions on the Msystems is

$$\varepsilon^P_{ij} = \sum_{k=1}^{M} \gamma^{(k)}\alpha^{(k)}_{ij} \text{ where } \alpha^{(k)}_{ij} = \left(m^{(k)}_i s^{(k)}_j + m^{(k)}_j s^{(k)}_i\right) \Big/ 2 \tag{3.1}$$

The shear stress acting on the k^{th} system is $\tau^{(k)} = \sigma_{ij}\alpha^{(k)}_{ij}$, and its sign determines the direction of slip. We will limit our attention to single crystals, such as the FCC Cu, which have slips systems that are crystallographically identical.

For each slip system, only two slip gradients will be considered. The gradient of slip normal to the slip plane does not induce plastic incompatibility (dislocation storage due to gradients or, in other words, a contribution to the Nye tensor) and will be ignored. The other two gradients, one in the direction of $s^{(k)}_j$ and the other in the perpendicular direction of $r^{(k)}_j$ (with $\mathbf{r} = \mathbf{m} \times \mathbf{s}$), are

$$\gamma^{(k)}_{,s} = \gamma^{(k)}_{,j} s^{(k)}_j \text{ and } \gamma^{(k)}_{,r} = \gamma^{(k)}_{,j} r^{(k)}_j \tag{3.2}$$

The plastic strain gradient is related to the slip gradients by

$$\varepsilon^P_{ij,m} = \sum_{k=1}^{M} \left(\gamma^{(k)}_{,s} s^{(k)}_m + \gamma^{(k)}_{,r} r^{(k)}_m\right)\alpha^{(k)}_{ij} \tag{3.3}$$

although the unknown variables in the theories are the slip gradients themselves, not $\varepsilon^P_{ij,m}$.

Additional notation is needed. Let $\dot{\rho}$ be the magnitude of the slip increment, i.e.,

$$\dot{\rho}^{(k)} = \left|\dot{\gamma}^{(k)}\right| \text{ With } \rho^{(k)} = \int \dot{\rho}^{(k)} = \int \left|\dot{\gamma}^{(k)}\right| \tag{3.4}$$

which is non-negative, non-decreasing, and often referred to as the accumulated slip. Introduce a combined, or effective, slip gradient on each of the systems with equal weighted contributions from the two gradients as

$$\Gamma^{(k)}_{eff} = \sqrt{\gamma^{(k)\,2}_{,s} + \gamma^{(k)\,2}_{,r}} = \sqrt{\gamma^{(k)}_{,\beta}\gamma^{(k)}_{,\beta}}, \tag{3.5}$$

where $(\ )_{,\beta}$denotes the gradient within the slip plane with respect to any orthogonal cartesian axes in the plane of the slip system and β is summed from 1 to 2. The equality of the two expressions above holds because $\gamma^{(k)}_{,\beta}\gamma^{(k)}_{,\beta}$ is invariant with respect to rotation of axes about the slip plane normal $\mathbf{m}^{(k)}$. The increment of this measure is

$$\dot{\Gamma}^{(k)}_{eff} = \left(\gamma^{(k)}_{,s}\dot{\gamma}^{(k)}_{,s} + \gamma^{(k)}_{,r}\dot{\gamma}^{(k)}_{,r}\right)\Big/\Gamma^{(k)}_{eff} = \gamma^{(k)}_{,\beta}\dot{\gamma}^{(k)}_{,\beta}\Big/\Gamma^{(k)}_{eff}. \tag{3.6}$$

A different effective slip gradient appears in the formulation of the non-incremental version. For this purpose, define an effective incremental slip gradient as

$$\dot{G}^{(k)}_{eff} = \sqrt{\dot{\gamma}^{(k)\,2}_{,s} + \dot{\gamma}^{(k)\,2}_{,r}} = \sqrt{\dot{\gamma}^{(k)}_{,\beta}\dot{\gamma}^{(k)}_{,\beta}}, \tag{3.7}$$

and the corresponding accumulated effective slip gradient as $G^{(k)}_{eff} = \int \dot G^{(k)}_{eff}$. Both measures of effective slip gradient are non-negative, but $G^{(k)}_{eff}$ is non-decreasing, while $\Gamma^{(k)}_{eff}$ can increase or decrease. They coincide when the deformation is proportional.

Each of the two versions of the theory presented below fits within the following analytical structure (Gudmundson, 2004, Gurtin and Anand, 2009, Fleck et al., 2015). Denote the volume of the body by V, its surface by S, and the outward unit normal to the surface at any point by n_j. For the theories under consideration, the primary unknown variables are the three displacements and the slips $\left(u_i, \gamma^{(k)}\right),\ i = 1,3,\ k = 1,M$. For both versions of the theories, the incremental change in the energy within the body (recoverable and unrecoverable) due to incremental forces acting on the surface of the body has the general form

$$\begin{aligned} \dot U &= \int_V \left\{ \sigma_{ij}\dot\varepsilon^e_{ij} + \sum_k \left(q^{(k)}\dot\gamma^{(k)} + q_s^{(k)}\dot\gamma^{(k)}_{,s} + q_r^{(k)}\dot\gamma^{(k)}_{,r} \right) \right\} dV \\ &= \int_V \left\{ -\sigma_{ij,j}\dot u_i + \sum_k \left(q^{(k)} - \tau^{(k)} - q^{(k)}_{s,s} - q^{(k)}_{r,r} \right)\dot\gamma^{(k)} \right\} dV \\ &\quad + \int_S \left\{ \sigma_{ij} n_j \dot u_i + \sum_k \left(q_s^{(k)} s_j^{(k)} + q_r^{(k)} r_j^{(k)} \right) n_j \dot\gamma^{(k)} \right\} dS \end{aligned} \tag{3.8}$$

where the stress variables are σ_{ij}, $q^{(k)}$, $q_s^{(k)}$, and $q_r^{(k)}$. It follows from (3.8) that equilibrium within V requires

$$\sigma_{ij,j} = 0 \tag{3.9}$$

and, for all active systems (i.e., $\dot\gamma^{(k)} \neq 0$),

$$q^{(k)} = \tau^{(k)} + q^{(k)}_{s,s} + q^{(k)}_{r,r} = \tau^{(k)} + q^{(k)}_{\beta,\beta} \tag{3.10}$$

In addition, the conjugate pairs for specifying surface boundary conditions are

$$\left(\sigma_{ij}n_j, \dot u_i\right) \text{ and } \left(\left(q_s^{(k)} s_j^{(k)} + q_r^{(k)} r_j^{(k)} \right) n_j,\ \dot\gamma^{(k)} \right)\ k = 1,M \tag{3.11}$$

Strictly, the sums in (3.8) extend only over the active systems, but they can be extended over all systems, because the inactive systems make no contribution.

3.2.1. *The incremental version*

The yield stress of the k^{th} system in the current state is a positive quantity denoted by $\tau_Y^{(k)}$, with $\tau_Y^{(k)} = \tau_Y^0$ prior to any plastic deformation for crystals such as FCC with identical slip systems. For simplicity, Bauschinger effects will not be considered, such that constraints on yielding on the k^{th} system are

$$\dot\gamma^{(k)} = 0 \text{ if } \left|q^{(k)}\right| < \tau_Y^{(k)},\quad \dot\gamma^{(k)} \geq 0 \text{ if } q^{(k)} = \tau_Y^{(k)},\quad \dot\gamma^{(k)} \leq 0 \text{ if } q^{(k)} = -\tau_Y^{(k)} \tag{3.12}$$

where $q^{(k)}$ is defined in (3.10). The incremental version reduces to the classical theory when slip gradients are omitted.

Slip gradients enter the incremental formulation only through the recoverable energy density

$$\psi = \frac{1}{2} L_{ijmn}\varepsilon^e_{ij}\varepsilon^e_{mn} + \frac{\tau_Y^0}{N+1}\sum_k \left(\ell\Gamma^{(k)}_{eff} \right)^{N+1} \tag{3.13}$$

Other forms for the slip gradient contribution to the recoverable energy could be considered, but this power law form is suitable for this study. The two additional parameters introduced in (3.13) are the material length parameter, ℓ, and the dimensionless gradient hardening parameter, N. An increment of recoverable energy due to increments of displacement and slip is

$$\dot\psi = \sigma_{ij}\dot\varepsilon^e_{ij} + \ell\tau_Y^0 \sum_k \left(\ell\Gamma^{(k)}_{eff} \right)^N \gamma^{(k)}_{,\beta}\dot\gamma^{(k)}_{,\beta} \Big/ \Gamma^{(k)}_{eff} = \sigma_{ij}\dot\varepsilon^e_{ij} + \sum_k q^{(k)}_\beta \dot\gamma^{(k)}_{,\beta} \tag{3.14}$$

where

$$\left(q_s^{(k)}, q_r^{(k)}\right) = \ell\tau_Y^0 \left(\ell\Gamma^{(k)}_{eff}\right)^N \left(\gamma^{(k)}_{,s}, \gamma^{(k)}_{,r}\right) \Big/ \Gamma^{(k)}_{eff} \text{ or } q^{(k)}_\beta = \ell\tau_Y^0 \left(\ell\Gamma^{(k)}_{eff}\right)^N \gamma^{(k)}_{,\beta} \Big/ \Gamma^{(k)}_{eff} \tag{3.15}$$

The increment of unrecoverable dissipation density is non-negative and given by

$$\dot D = \sum_k \tau_Y^{(k)} \dot\rho^{(k)} \tag{3.16}$$

Thus, the increment of energy change in the body (recoverable and unrecoverable) is

$$\dot{U} = \int_V \{\dot{\psi} + \dot{D}\} dV = \int_V \left\{ \sigma_{ij}\dot{\varepsilon}_{ij}^{e} + \sum_k \left(\tau_Y^{(k)}\dot{\rho}^{(k)} + q_\beta^{(k)}\dot{\gamma}_{,\beta}^{(k)} \right) \right\} dV \tag{3.17}$$

The functional characterizing the quadratic incremental terms in the energy change is

$$\Phi = \frac{1}{2}\int_V \left\{ \dot{\sigma}_{ij}\dot{\varepsilon}_{ij}^{e} + \sum_k \left(\dot{\tau}_Y^{(k)}\dot{\rho}^{(k)} + \dot{q}_\beta^{(k)}\dot{\gamma}_{,\beta}^{(k)} \right) \right\} dV \tag{3.18}$$

The incremental hardening law for the slip systems is taken to be (Hill, 1966)

$$\dot{\tau}_Y^{(j)} = \sum_k h_{jk}\dot{\rho}^{(k)} \tag{3.19}$$

where the constant hardening matrix, h_{jk}, is positive definite. This is one of many possible choices that have been proposed for classical single crystal plasticity. A direct calculation gives

$$\dot{q}_\beta^{(k)}\dot{\gamma}_{,\beta}^{(k)} = \sum_{j,k} \ell^{1+N}\tau_Y^0 {\Gamma_{eff}^{(k)}}^{(N-1)} \left(\dot{\gamma}_{,\beta}^{(k)}\dot{\gamma}_{,\beta}^{(k)} + (N-1){\dot{\Gamma}_{eff}^{(k)}}^2 \right) \tag{3.20}$$

It follows that the quadratic functional (3.18) governing the quadratic terms for the energy change in the incremental boundary problem for this version of SGP is

$$\Phi = \frac{1}{2}\int_V \left\{ \dot{\sigma}_{ij}\dot{\varepsilon}_{ij}^{e} + \sum_{j,k} h_{jk}\dot{\rho}^{(j)}\dot{\rho}^{(k)} + \sum_k \ell^{1+N}\tau_Y^0 {\Gamma_{eff}^{(k)}}^{(N-1)} \left(\dot{\gamma}_{,\beta}^{(k)}\dot{\gamma}_{,\beta}^{(k)} + (N-1){\dot{\Gamma}_{eff}^{(k)}}^2 \right) \right\} dV \tag{3.21}$$

This functional should be regarded as dependent on increments of displacement and slips with $\dot{\varepsilon}_{ij}^{e} = \left(\dot{u}_{i,j} + \dot{u}_{j,i}\right)/2 - \sum_k \dot{\gamma}_k \alpha_{ij}^{(k)}$. Although it is not necessarily a good physical choice, for mathematical simplicity, the special case, $N = 1$, has been employed in some earlier literature, for which the slip gradient terms simplify to $\sum_k \ell^2 \tau_Y^0 \dot{\gamma}_{,\beta}^{(k)}\dot{\gamma}_{,\beta}^{(k)}$. For incremental boundary value problems, Φ must be augmented by quadratic incremental contributions representing the work done at the surface (or possibly body forces) to form the quadratic functional characterizing the incremental system energy.

3.2.2. The non- incremental version

The non-incremental version also reduces to the classical theory for independently hardening single crystals when the slip gradients are omitted. In the following non-incremental formulation (see also Nellemann, Niordson & Nielsen (Nellemann et al., 2017) for a detailed development of the incremental version), there is no gradient contribution to the recoverable energy although such a contribution could be included. The slip gradients enter the formulation only through the unrecoverable energy density and are thus intrinsically dissipative in nature. This version is constructed so that it coincides with the incremental version when the plastic deformation is proportional, as defined more fully below.

The only recoverable energy density in this version is $\psi = L_{ijmn}\varepsilon_{ij}^{e}\varepsilon_{mn}^{e}/2$. The dissipation rate, or unrecoverable energy rate, must be non-negative. Here we invoke an unusual construction proposed by Gudmundson (Gudmundson, 2004) and Gurtin and Anand (Gurtin and Anand, 2005), which insures non-negative dissipation. Specifically, the dissipation rate is chosen as

$$\dot{D} = \sum_k \left\{ \tau_Y^{(k)}\dot{\rho}^{(k)} + q_\beta^{(k)}\dot{\gamma}_{,\beta}^{(k)} \right\} \tag{3.22}$$

with $\dot{\tau}_Y^{(j)} = \sum_k h_{jk}\dot{\rho}^{(k)}$ as before, and higher order stresses that depend on the *slip gradient increments* according to

$$q_\beta^{(k)} = \ell\tau_Y^0 \left(\ell G_{eff}^{(k)}\right)^N \dot{\gamma}_{,\beta}^{(k)} \Big/ \dot{G}_{eff}^{(k)} \tag{3.23}$$

This choice ensures a non-negative dissipation rate,

$$\dot{D} = \sum_k \left\{ \tau_Y^{(k)}\dot{\rho}^{(k)} + \ell\tau_Y^0 \left(\ell G_{eff}^{(k)}\right)^N \dot{G}_{eff}^{(k)} \right\} \geq 0 \tag{3.24}$$

For the non-incremental version, the expression (3.8) for $\dot{U}$still holds, as do the equilibrium and yield conditions, (3.9)-(3.12). However, it is not possible to write a functional characterizing the quadratic incremental terms in the energy change for the non-incremental theory (and, hence, the terminology ‘non-incremental’). For the rate-independent non-incremental version, the stress quantities $\left(q^{(k)}, q_\beta^{(k)}\right)$ themselves are not known in the current state since they depend on the specific traction and/or displacement increments imposed on the surface of the solid. In other words, at any step in the loading process where the loads undergo a non-proportional incremental change, these stress quantities will generally undergo discontinuous changes. These discontinuities can, in turn, lead to unphysical elastic gaps in some problems. The solution procedure for non-incremental problems has been laid out by Fleck and Willis (Fleck and Willis, 2009) for both rate-independent and rate-dependent behavior. The rate-dependent formulation,

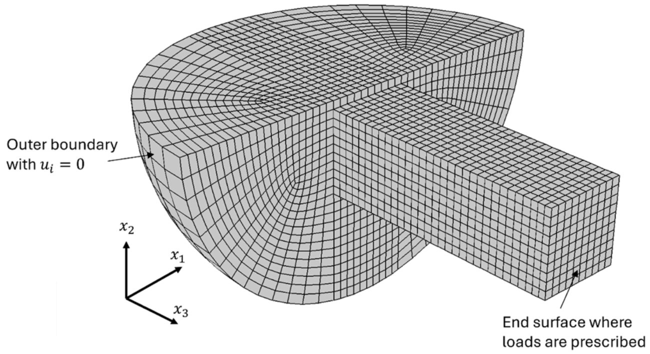

Fig. 6. A full 3D finite element model of the experimental configuration: a one-end-attached square cantilever beam. Mesh used for classical crystal plasticity simulations is shown here.

which will be used in this paper, smooths out the discontinuous changes in $\left(q^{(k)}, q_{\beta}^{(k)}\right)$ when non-proportional loading occurs, but it does not eliminate the fundamental differences in the two versions, as will be discussed further for the orthogonal-bend test.

We elaborate on the notion of proportional loading as relevant to the current study. A *proportional plastic loading* increment in the context of single crystal SGP is defined as follows, in more detail than stated earlier. Let λ be a monotonically increasing loading parameter which starts from zero at the onset of loading with $\dot{\lambda}$ as an imposed increment. Denote the distribution of plastic slips and their gradients in the current state by $\left(\gamma^{(k)}, \gamma_{,\beta}^{(k)}\right)$. If the distribution of all the increments of the slips and their gradients in the next step has the form $\left(\dot{\gamma}^{(k)}, \dot{\gamma}_{,\beta}^{(k)}\right) = c\dot{\lambda}\left(\gamma^{(k)}, \gamma_{,\beta}^{(k)}\right)$ where c is a multiplicative constant, the step is proportional. If such a relationship holds for all the steps starting at $\lambda = 0$, the deformation is said to be proportional loading. The simplest examples of boundary value problems which can display strict proportionality are pure power-law materials for which the linear elastic contribution is neglected. For problems satisfying proportional loading, it is easy to show that the stress quantities $\left(q^{(k)}, q_{\beta}{}^{(k)}\right)$ for the non-incremental and incremental versions coincide, and the entire solutions for the two versions coincide. Even if there is some departure from proportionality, predictions from the two versions will often be reasonably close to each other. When an abrupt non-proportional step in the loading occurs, major differences can arise.

A rate-dependent version of a non-incremental strain gradient crystal plasticity has been implemented into an in-house finite element solver. The purpose of the numerical implementation is to simulate the orthogonal cantilever bend experiments. The implementation differs somewhat from the formulation given above but the essence is the same, as will be apparent when solutions to a pure bend case are compared to the incremental version. Details of the implementation will not be covered here. The implementation follows the kinematics as described in Bardella and Niordson (Bardella and Niordson, 2020), and the constitutive description relies on a viscoplastic response function that was introduced for isotropic strain gradient plasticity by Dahlberg and Faleskog (Dahlberg and Faleskog, 2013) and used, e.g., in Dahlberg and Boåsen (Dahlberg and Boåsen, 2019) to model small scale bending and in Dahlberg and Ortiz (Dahlberg and Ortiz, 2020) to model micropillar compression experiments. For completeness, some details of the implementation can be found in the supplementary material.

Comparisons of the predictions from the incremental rate-independent model and the non-incremental rate-dependent model for orthogonal pure bending were presented in Section 2 in Figs. 2, 3 & 4. Apart from the small elastic gap and the more extended region of reduced plasticity for the case of κ_1 held constant in Stage 2, the two sets of predictions are similar, subject to an appropriate choice of hardening law. The 3D simulations of the sequential orthogonal cantilever bending experiments were carried out using a code based on the non-incremental theory.

3.3. Finite element simulation of the experiments

Full 3D finite element models of the experimental geometries were created. The cantilever beam and a region of the support were modeled to more accurately reflect the clamping at one end of the beam. The support was modeled out to about 2 times w from the cantilever beam root, cf., Fig. 6. Zero displacements were prescribed at the outer boundary of this region. The length of the beam corresponded to the cantilever load length, l_L. The details of the cantilever-indenter contact, including the W tabs and the Si actuator, were not included in the model. Loading on the beam was introduced by prescribing either displacement or nodal forces on all nodes of the square surface at the end of the beam. Nodal forces were applied, consistent with the shape function interpolation, to represent an evenly distributed traction vector. The resulting stress distribution in that cross section, from this method of load application, is not an entirely correct representation of the actual stress due to the applied loading through the W tab. As the plastic deformation zone is located at the clamped end of the cantilever, well away from the loading surface, the sensitivity to the specific nodal force distribution used is minimal, in accordance with Saint-Venant's principle. No constraints on plastic slip were prescribed for the higher order continuum model.

Two different modelling approaches have been used. A classic crystal plasticity finite element (CPFE) model was first used to fit the

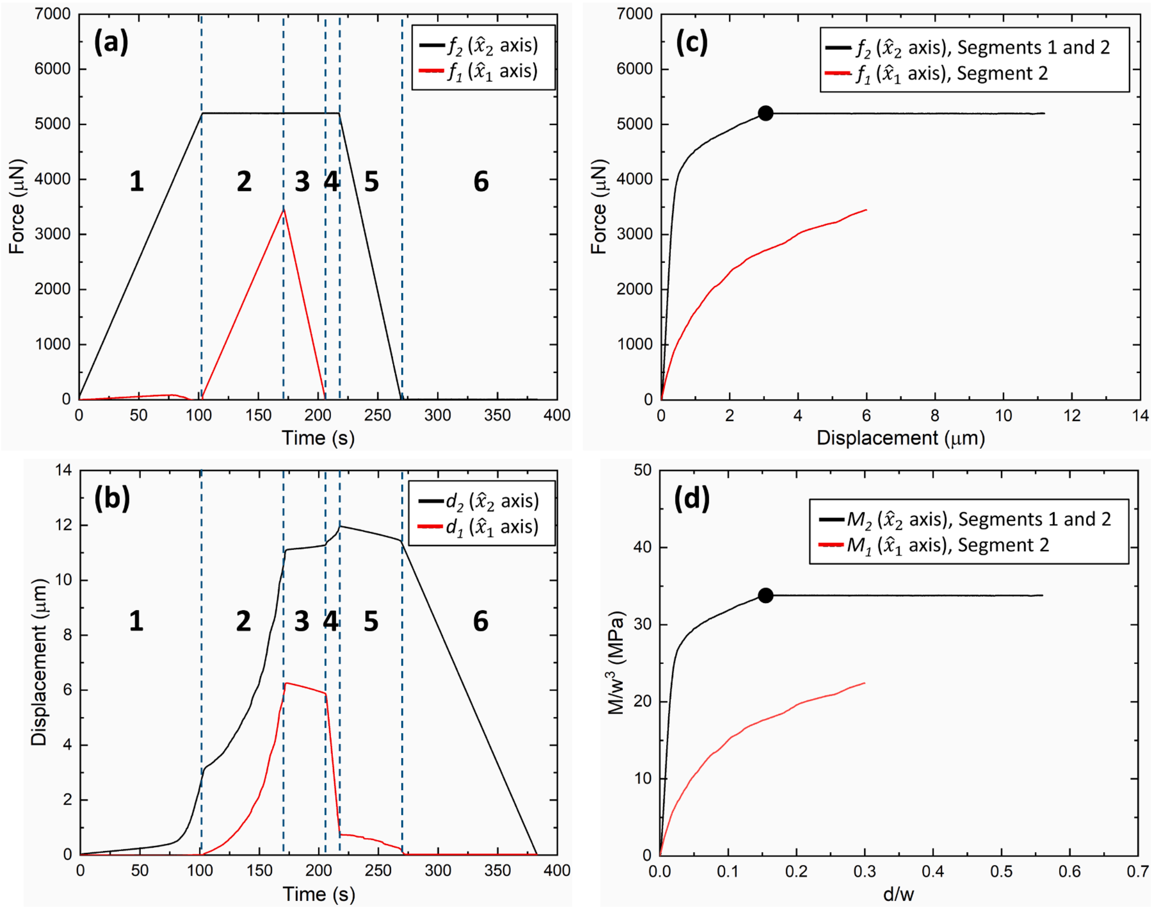

Fig. 7. Sequential cantilever orthogonal bending with loading in $-x_2$ and $+x_1$ directions both in force control: (a) force – time sequence for both $-x_2$ and $+x_1$ axes; (b) the corresponding displacement – time sequence for both $-x_2$ and $+x_1$ axes; (c) plots of measured bending force vs. actuator displacement for both $-x_2$ and $+x_1$ axes in Stages 1 and 2; (d) data shown in (c) plotted as scaled bending moment vs. scaled displacement. Dashed lines and numbers in (a) and (b) highlight Segments 1 – 6 described in the text. The black dots in (c) and (d) denote the transition from Stage 1 to Stage 2.

initial value for the critical resolved shear stress τ_0 for the largest beam, since $w = 20$ μm is much larger than the expected best fit value for the material length parameter. The crystal plasticity model was run in Abaqus with the Damask crystal plasticity framework. The constitutive description was kept simple in anticipation of the gradient plasticity modelling. The Hill flow rule (Hill, 1966) and Peirce, Asaro and Needleman hardening law (Peirce et al., 1983) were used. Anisotropic elastic constants for single crystal Cu were taken from Hirth and Lothe (Hirth and Lothe, 1982) ($C_{11} = 168.4$ GPa, $C_{12} = 121.4$ GPa and $C_{44} = 75.4$ GPa) and used throughout. A good fit to the initial yield behavior was found using $\tau_0 = 40$ MPa. The CPFE solution also served as a check on the strain gradient crystal plasticity (SGCP) code to make sure that the predictions of the SGP model approach those of the conventional crystal plasticity when w becomes large. Due to a high computational cost, the finite element mesh used for the SGCP model used a graded element size along the beam length with the smallest elements at the beam root. The beam cross section was modeled by 10 by 10 elements, and the length of the beam was resolved by 10 elements of increasing size in a geometric progression (ratio 1.222). Further details of the implementation of the two theories for numerical solution of the pure orthogonal-bend problem and the orthogonal-bend cantilever problem are given in Section S6 of the SI document.

4. Results and discussions

4.1. Experimental results

Fig. 7 illustrates the cantilever sequential orthogonal bending experiments in which the initial $-x_2$ direction loading and the subsequent $+x_1$ direction loading were executed both in force control. A 20 μm square Cu <100> cantilever was used. Fig. 7(a) shows a time history of $-x_2$ direction force (f_2) and $+x_1$ direction force (f_1) in segments. Fig. 7(b) shows the time history of $-x_2$ direction displacement (d_2) and $+x_1$ direction displacement (d_1) in corresponding segments. In Fig. 7(a), Segment 1 shows a constant-rate

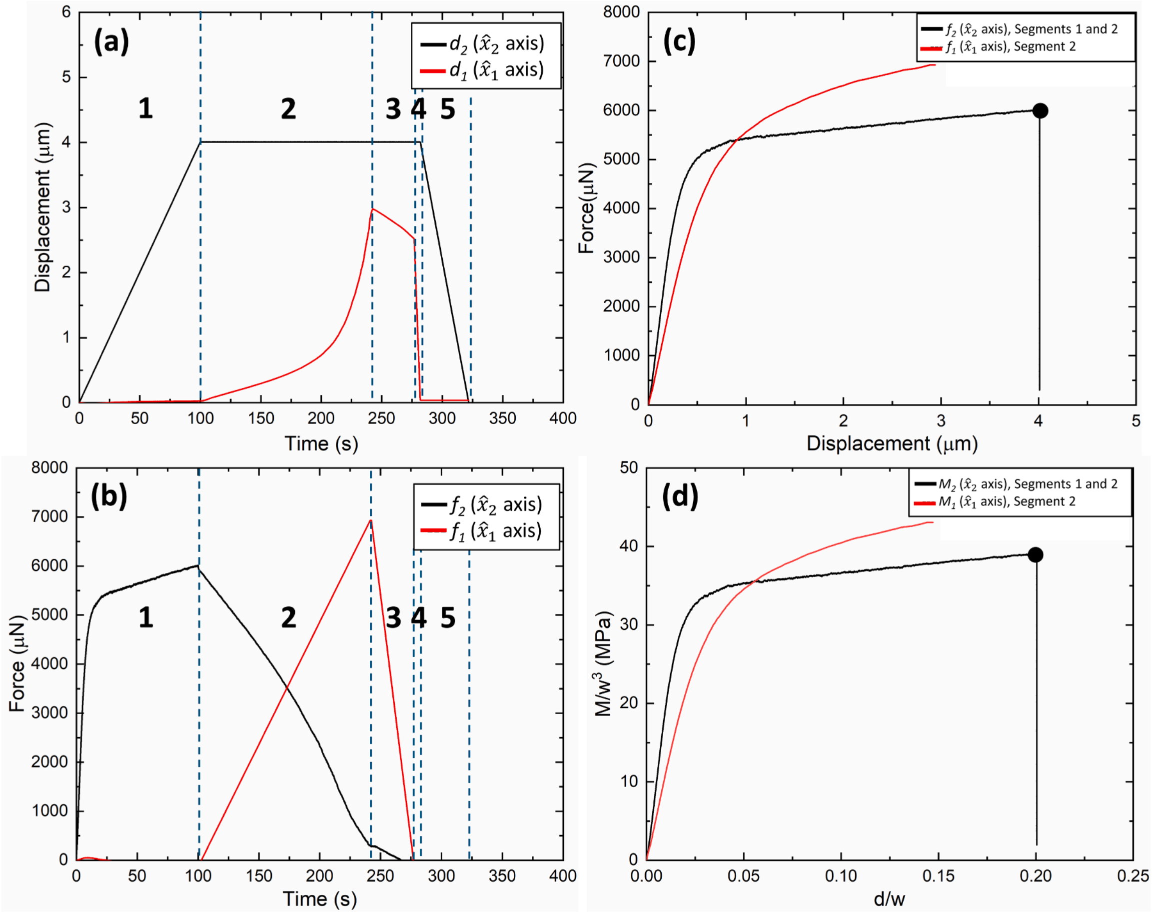

Fig. 8. Sequential cantilever orthogonal bending with loading in $-x_2$ direction in displacement control and $+x_1$ direction in force control: (a) displacement – time sequence for both $-x_2$ and $+x_1$ axes; (b) the corresponding force – time sequence for both $-x_2$ and $+x_1$ axes; (c) plots of measured bending force vs. actuator displacement for both $-x_2$ and $+x_1$ axes in Stages 1 and 2; (d) data shown in (c) plotted as scaled bending moment vs. scaled displacement. Dashed lines and numbers in (a) and (b) highlight Segments 1 – 5 described in the text. The black dots in (c) and (d) denote the transition from Stage 1 to Stage 2.

increase in f_2 only (0 - 103 s). Segment 2 shows a constant-rate increase in f_1, with f_2 held constant (103 - 171 s). Segment 3 shows a constant-rate decrease of f_1 to zero, with f_2 held constant (171 - 206 s). In Segment 1, f_2 (Fig. 7(a)) and d_2 (Fig. 7(b)), combined, give cantilever's response to bending in $-x_2$ direction. In Segment 2, f_1 and d_1, combined, give cantilever's response to bending in $+x_1$ direction while the $-x_2$ direction load was held constant. In Segment 3, f_1 and d_1, combined, give cantilever's response to $+x_1$ direction unloading to zero load while the $-x_2$ direction load persists. It should be noted that d_2 continues to increase in Segments 2 and 3 at fixed f_2, because the resultant force, $f = \sqrt{f_2^2 + f_1^2}$, continues to increase beyond the maximum value of f_2 at the end of Segment 1 and the combination of constant vertical force and increasing horizontal force activates plastic slip with a component in the vertical direction. It should also be noted that there is no relative displacement between the Si actuator and the cantilever in Segments 1 – 3. In Segment 4, d_1 decreased at a constant rate to 0.75 μm, with f_2 held constant (206 - 217 s). During the actuator withdrawal in $+x_1$ direction, there was a relative displacement between the Si actuator and the cantilever in the $+x_1$ direction. Due to the presence of f_2, this $+x_1$ direction withdrawal incurred a frictional force in the $-x_1$ direction ($f_1 < 0$, not shown in Fig. 7(a)) and a consequent increase in the resultant force f, leading to a further increase in d_2. Segment 5 in Fig. 7(a) shows a constant-rate decrease of f_2 to zero, with a simultaneous decrease of d_1 to zero. Segment 6 shows a final constant-rate decrease of d_2 to zero.

While Figs. 7(a) and 7(b) illustrate the entire test sequence, we recall that the focus of this study is to gauge the cantilever response when the bending load changes in a non-proportional manner in Segments 1 and 2, which coincide with the Stage 1 and Stage 2 described in the conceptualization section (Section 2). Thus, data associated with Segments 3 and higher, describing the cantilever unloading behavior in the $+x_1$ direction and the subsequent actuator withdrawal in both x_1 and x_2 directions, are of minimal interest for the purpose of the present paper. Therefore, we replot in Fig. 7(c) the data displayed in Figs. 7(a) and 7(b) as f_2 vs. d_2 and f_1 vs. d_1, superimposed, showing only data segments 1 and 2, i.e., cantilever response to Stage 1 and Stage 2 loading. The $-x_2$ direction data generated in Stage 2 are easily distinguished from that generated in Stage 1, because of the constant f_2 value. Fig. 7(d) replots the raw

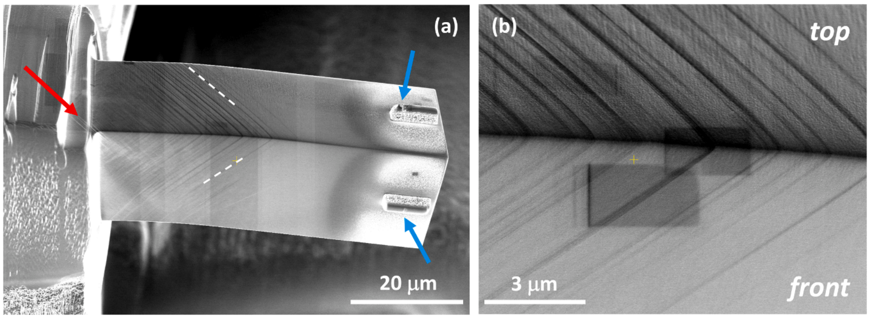

Fig. 9. Typical morphologies of Cu <100> square cantilevers after sequential orthogonal bending: (a) overview of one 20 μm cantilever after sequential bending in $-x_2$ and $+x_1$ directions; (b) a higher magnification image of the surface slip steps shown in (a). The dimensions of the W tabs are 2 μm × 2 μm × 10 μm. The blue arrows in (a) highlight the contact marks on the W tabs. The red arrow and white dashed lines in (a) highlight the surface slip steps. Bending was conducted under force control in both $-x_2$ and $+x_1$ directions.

data shown in Fig. 7(c) as scaled bending moment vs. scaled actuator displacement, M_2/w^3 vs. d_2/w and M_1/w^3 vs. d_1/w, superimposed, again with only data segments 1 and 2 displayed. The bending moments are $M_2 = f_2 \times l_L(x_2)$ and $M_1 = f_1 \times l_L(x_1)$, with $l_L(x_2)$ and $l_L(x_1)$ being, respectively, the x_2 and x_1 direction load length. This scaling ensures that, for cantilevers with fixed dimension ratios (l:w:t = 3:1:1 in the present experiments), the scaled bending response, M/w^3 vs. d/w, should be independent of cantilever size for any conventional plasticity theory having no dependence on a material length scale parameter. The same control sequence and data acquisition procedure were applied to all orthogonal cantilever bending experiments in which both $-x_2$ and $+x_1$ direction loadings were executed in load control.

Fig. 8 illustrates the cantilever sequential orthogonal bending experiments in which the initial $-x_2$ direction loading was executed in displacement control and the subsequent $+x_1$ direction loading were executed in load control. Another 20 μm square Cu <100> cantilever was used, again with its crystal axes aligned with the specimen axes.

Fig. 8(a) shows a time history of d_2 and d_1 in segments. Fig. 8(b) shows the time history of f_2 and f_1 in corresponding segments. In Fig. 8(a), Segment 1 shows a constant-rate increase in d_2 only (0 - 103 s). Segment 2 shows a constant-rate increase in f_1, with d_2 held constant (103 - 242 s). Segment 3 shows a constant-rate decrease of f_1 to zero, with d_2 held constant (242 - 277 s). In Segment 1, d_2 (Fig. 8(a)) and f_2 (Fig. 8(b)), combined, give cantilever's response to bending in $-x_2$ direction. In Segment 2, d_1 and f_1, combined, give cantilever's response to bending in $+x_1$ direction with $-x_2$ direction displacement held constant. In Segment 3, d_1 and f_1, combined, give cantilever's response to $+x_1$ direction unloading to zero load with the $-x_2$ direction displacement fixed. It should be noted that, with d_2 fixed in Segments 2 and 3, f_2 decreases continuously ($-x_2$ direction force continues to unload from the start of $+x_1$ direction loading). Unlike the behavior in the previous test, maintaining a constant vertical end-displacement in Segment 2 causes the magnitude of the vertical force to decrease even though the horizontal end-displacement is increasing. It is again noted that there is no relative displacement between the Si actuator and the cantilever in Segments 1 – 3. In Segment 4, d_1 decreased at a constant rate to zero, with d_2 held constant (277 - 282 s). In Segment 5, d_2 decreases at a constant rate to zero (282 - 322 s). Again, Fig. 8(c) replots the data shown in Figs. 8(a) and 8(b) as f_2 vs. d_2 and f_1 vs. d_1, superimposed, showing only data segments 1 and 2, i.e., cantilever response to Stage 1 and Stage 2 loading. The $-x_2$ direction data generated in Segments 2 are easily distinguished from that generated in Segment 1, because of the constant d_2 value (the vertical load-drop in Fig. 8(c)). Fig. 8(d) again replots the raw data shown in Fig. 8(c) as scaled bending moments scaled actuator displacement, M_2/w^3 vs. d_2/w and M_1/w^3 vs. d_1/w, superimposed, again with only data segments 1 and 2 displayed. The same control sequence and data acquisition procedure were applied to all cantilever double bending experiments in which the initial $-x_2$ direction loading was executed in displacement control and the subsequent $+x_1$ direction loading was executed in load control.

Fig. 9 shows typical morphologies of Cu <100> square cantilevers after sequential orthogonal bending. Fig. 9(a) shows an overview of one 20 μm cantilever after sequential bending in $-x_2$ and $+x_1$ directions under force control, again with the Cu crystal axes aligned with specimen axes. The blue arrows in Fig. 9(a) highlight the contact marks on the W tabs, from which load lengths $l_L(x_2)$ and $l_L(x_1)$ were measured. The surface slip steps, one set of which is highlighted by the white dashed lines in Fig. 9(a), provides definitive evidence of plastic deformation occurring due to the bending loads in $-x_2$ and $+x_1$ directions. Some slip steps extend into the cantilever attachment region, as highlighted by the red arrow in Fig. 9(a), indicating that limited plasticity occurred in the attachment region. Fig. 9(b) shows a higher magnification image of the surface slip steps highlighted in Fig. 9(a), which resulted from the same set of Cu {111} planes intersecting the cantilever top and front surfaces. Figs. 10(a) and 10(b) show, respectively, overviews of one 5 μm Cu <100> square cantilever and one 2 μm Cu <100> square cantilever after sequential bending in $-x_2$ and $+x_1$ directions under force control. Figs. 10(c) and 10(d) show, respectively, higher magnification images of the surface slip steps on the top and front surfaces of the 5 μm and 2 μm cantilevers. At all three cantilever sizes, it is evident that the same set of surface slip steps was observed.

Fig. 11 shows measured responses of 20 μm Cu <100> square cantilevers to sequential orthogonal bending. Fig. 11(a) plots M/w^3 vs. d/w for x_2-axis and x_1-axis, superimposed, with only Stage 1 and Stage 2 data displayed. Loadings for both x_2-axis and x_1-axis were executed under force control. Fig. 11(b) plots M/w^3 vs. d/w for x_2-axis and x_1-axis, superimposed, with only Stage 1 and Stage 2 data displayed. Loading for x_2-axis was executed under displacement control and loading for x_1-axis was executed under force control. Several statements can be made by comparing results shown in Figs. 11(a) and 11(b). First, collected data show reasonable repeatability under both loading scenarios. Second, responses to the initial single-axis bending, M_2/w^3 vs. d_2/w, show reasonable agreement under both loading scenarios. Third, responses to the subsequent bending, M_1/w^3 vs. d_1/w, show marked differences between force and displacement control. In the second loading scenario, the x_2-axis unloads as soon as the x_1-axis load is applied (Fig. 8 (b), Segments 2 and 3), which does not occur in the first loading scenario. Considerably more plastic deformation in both the vertical and horizontal directions occurs in the first loading scenario, particularly in the early portion of Stage 2. Under both loading scenarios, the early bending response in x_1-direction is significantly less stiff than the initial elastic bending response in x_2-direction.

Fig. 12 shows responses of different sized Cu <100> square cantilevers to sequential orthogonal bending with x_2-axis and x_1-axis loadings both executed under force control, again plotted as M/w^3 vs. d/w for x_2-axis and x_1-axis, superimposed, with only Stage 1 and Stage 2 data displayed. Dotted and solid lines again show, respectively, responses in x_2 and x_1 directions. Lines colored in blue, red, and black, denote, responses measured from 2 μm, 5 μm, and 20 μm beams, respectively. Different lines represent results of separate tests, each using a new cantilever beam specimen. A significant size effect is displayed in Fig. 12 as the cantilever size decreases from 20 μm to 2 μm, for both x_2-axis and x_1-axis bending. At all cantilever sizes, the early bending response in x_1-direction is significantly less stiff due to the plasticity contribution than the initial elastic bending response in x_2-direction.

4.2. Simulations of orthogonal bending of the cantilevers

The SGCP model formulated using the non-incremental theory was calibrated against experimental results from all three cantilever beam sizes. We employed an iterative fitting procedure to determine the initial yield stress τ_0, the material length scale ℓ, and hardening parameters h_0, τ_s, and η, as described in the SI document. All other constitutive parameters were held constant in the fitting process. Effort was concentrated on getting the first load application response to fit well and the second load stage response was only used to gauge the effect of the latent hardening parameter.

We note that this fitting procedure was not intended as a complete parameter optimization. Rather, the aim was to obtain a representative and consistent set of material parameters that give a good agreement across all specimen sizes. While alternative parameter combinations could give comparably good fits, particularly due to a mild trade-off between τ_0 and ℓ (increasing one while decreasing the other can produce similar responses for small perturbations around the reported values). The calibrated material parameters for the SGCP model are: $\tau_0 = 40$ MPa (as also determined using the conventional model), $\ell = 1.5$ μm, $h_0 = 35$ MPa, $\tau_s = 50$ MPa, and $\eta = 1.2$. The other constitutive parameters (not fitted) were $m = 100$, $\kappa = 10^{-3}$, $\dot{\gamma}_0 = 10^{-3}$ s^{-1}, and the elastic moduli listed earlier.

While some details of the solutions are different compared to the experiments, the overall behavior observed in the experiments is well reproduced by the SGCP model for all three beam sizes. For the simulations, we have focused on the force-control experiments (cf. Fig. 7 and the associated descriptions) rather than those under displacement-control (cf. Fig. 8 and the associated descriptions), because the former are the more difficult to replicate. In Fig. 13(a), the simulation results for normalized bending moments vs. normalized displacements at the tip of the cantilevers are plotted for both Stage 1 and Stage 2 loading as heavy lines. Superimposed in Fig. 13(a) are the experimental results displayed in Fig. 12, shown as light lines. Colors are used, similar to those in Fig. 12, to distinguish between different beam sizes.

The apparent elastic slope of the smallest beams in the experiment was markedly different from the larger ones. This difference is believed to be due to experimental complications and not a feature of the size dependent material behavior. As the cantilever width w decreases to 2 μm, conditions of contact between the actuator and the cantilever specimen may be different from those at larger cantilever sizes. The extent of plasticity occurring in the cantilever attachment region (see e.g., Fig. 9) may also change as w decreases to 2 μm. Therefore, the simulations do not reproduce that initial slope. Due to this, the point at which the loading changes from Stage 1 to Stage 2 for the smallest beams is more difficult to match to the experiments. The transition point was chosen just slightly after gross plastic flow commenced since that is believed to be the operative distinction.

As explained above, several material parameters were fitted against experimental data for x_2-axis loading during Stage 1. Consequently, the model reproduces the experimental behavior well in Stage 1, as evident in Fig. 13(a). During Stage 2, the x_2-direction force on the tip of the cantilever was kept constant and the x_1-direction force increased from zero. The transition from Stage 1 to Stage 2 is marked by a dot in Fig. 13(a). Beyond that point, the bending moment about the x_2-axis does not increase, and the flat portions of the curves are not indicative of a constitutive behavior but rather a result of the boundary conditions. The displacement d_2 along the x_2-direction continues to increase during Stage 2, and this is rather well captured for the two larger beams. But for the smallest beam with $w = 2$ μm, the model predicts less displacement in the x_2-direction. The model results for bending about the x_1-axis show behavior close to the experiment for the 20 μm beam. For the 5 and 2 μm beams, the model results for the x_1-axis bending in Stage 2 follow the general behavior of the experiments and the model produces a reasonable agreement with the entire experimental dataset. The model result for the 5 μm beam deviates after some deformation and is more compliant than the experiments, while that for the 2 μm beam appears to be more stiff than the experiments. To quantitatively compare the model and experiments, an offset line has been introduced in Fig 13(a). This line follows the elastic slope (of the simulations and experiments for the 20 μm and 5 μm beams) but is offset from the origin by 0.025. This offset value was chosen to be able to intersect all simulation and experiment curves on the same offset line, considering specifically that loading about the x_1-axis for the 2 μm beam experiments suffers from a smaller range of available data. The values for the normalized moment at the intersections with the offset line have been plotted against the beam size in Fig. 13(b). The experimental data is plotted using light colored dots and the model results are denoted by colored crosses. Data for both bending axes are superimposed in the same figure. As is evident from Fig. 13(b), the model does a good job of representing the experimental data and only the offset normalized moment value for the 2 μm beam about the x_1-axis is outside of the experimental

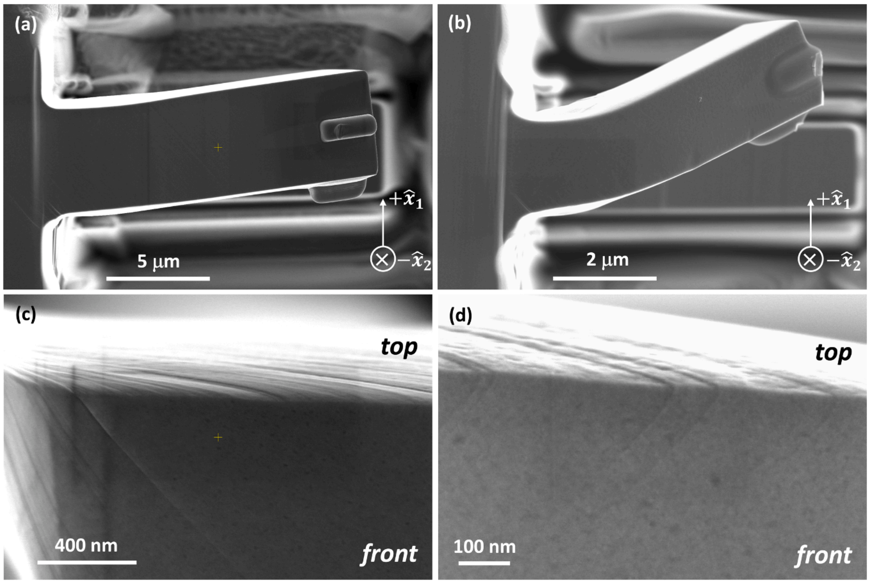

Fig. 10. Typical morphologies of Cu <100> square cantilevers after sequential orthogonal bending: (a/b) overviews of one 5 μm cantilever and one 2 μm cantilever after consecutive bending in $-x_2$ and $+x_1$ directions; (c/d) higher magnification images of the slip steps on 5 μm and 2 μm cantilever surfaces. Bending was conducted under force control in both $-x_2$ and $+x_1$ directions.

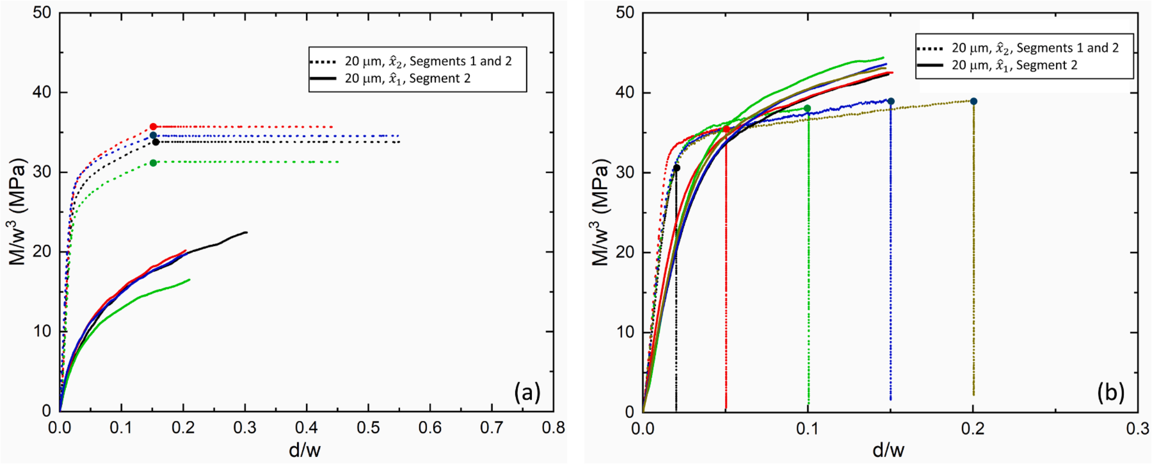

Fig. 11. Response of 20 μm Cu <100> square cantilevers to sequential orthogonal bending: superimposed x_2-axis and x_1-axis scaled bending moment vs. scaled displacement when (a) x_2-axis loading and x_1-axis loading were both executed under force control; (b) x_2-axis loading was executed under displacement control and x_1-axis loading was under force control. Dotted and solid lines denote, respectively, x_2-axis response and x_1-axis response. Different colored lines represent results of separate measurements. Dots in (a) and (b) again denote the transition from Stage 1 to Stage 2.

scatter. Even though these values are not a direct measure of the initial yield stress of the beams, they can be used to gauge the plastic size effect. Both experiments and model results show a clear size dependence, where smaller beams can sustain significantly higher stress before initiation of gross plastic deformation. The increase in stress from the 20 μm beams to the 2 μm beams is almost a factor of 3.

While not particularly conspicuous in Fig. 13(a), the slope of the moment around the x_1-axis after the transition from Stage 1 to Stage 2 is initially identical to the elastic slope. However, as is obvious from Fig. 13(a), this initial "elastic response" region seems to be of minor consequence in comparison to the full load history (similar to the pure bending simulations shown in Fig. 4). The conclusion is that *an elastic gap does appear* in sequential orthogonal bend non-proportional loading when the simulation is based on a non-incremental rate-dependent SGP theory, but the consequences of this, in comparison to experimental data, are relatively small in this particular loading configuration over the full range of loads considered. A second conclusion is that the work hardening representation in the model is important to accurately capture the extent of the plasticity on non-proportional load paths under force-

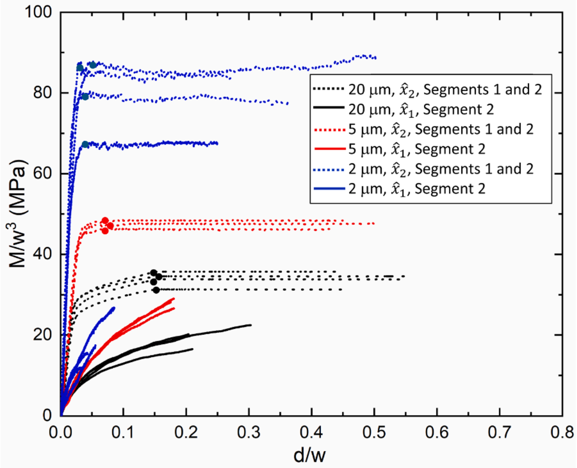

Fig. 12. Response of Cu <100> square cantilevers to sequential orthogonal bending: scaled bending moment plotted vs. scaled displacement. Dotted and solid lines show, respectively, scaled bending responses in x_2 and x_1 directions. Lines colored in blue, red, and black denote, respectively, responses measured from 2 μm, 5 μm, and 20 μm beams. Different lines denote results of separate runs. Bending was conducted under force control in both x_2 and x_1 directions.

control. This aspect has not been explored in this study.

4.3. *Additional discussions*

One comment may be offered regarding strength elevation due to dislocation source starvation and due to strain gradient strengthening. Micropillar compression tests have been studied extensively for strength elevation due to effects of dislocation nucleation, a.k.a. dislocation source starvation (Uchic et al., 2004, Greer and De Hosson, 2011). A key difference between uniaxial compression along the axis of straight micropillars and cantilever torsion or bending lies in that an elastic core exists in cantilever torsion or bending, and in contrast, this elastic core is absent in pillar compression experiments. As a result, the commonly observed “strain burst” phenomenon in micropillar compression—where motion of dislocations, once nucleated, along a single slip system across the entire specimen unimpeded—is absent in either L-beam torsion (Zhang et al., 2023) or the present orthogonal cantilever bending experiments (see e.g., Fig. 10). In the latter experiments, dislocations nucleated from one side of the specimen (the occurrence of which is clearly demonstrated through the surface slip steps shown in Figs. 9 and 10) cannot move across the entire specimen to the opposite side and escape due to the presence of the elastic core, and are trapped within the deformed specimen volume. The reasonable match between the present strain gradient crystal plasticity simulation outputs and the present cantilever orthogonal bending experimental data suggests that, while dislocation nucleation may influence the observed strength elevation, the interaction of dislocations contained within the deformed volume plays a significant role in the present cantilever orthogonal bending experiments.

5. Conclusions

Sequential orthogonal bending experiments on micron-scale Cu single crystal cantilever beams have been carried out with emphasis on the plastic behavior associated with non-proportional bending. To the best of our knowledge, the present experiments are the first involving deliberately imposed non-proportional loading involving sharp, non-collinear loading direction changes conflated with the strong size effect in the micron range due to plastic strain gradients. The experiments were designed to provide data that can be used as a reference to evaluate the predictive capabilities of micron scale elastic-plastic constitutive models, and they provide responses for geometries and in the range of strains relevant to micron-scale structural applications. In addition, this paper presents computational simulations of the experiments based on two formulations of single crystal strain gradient plasticity theory currently available, which are expected to differ significantly only when non-proportional deformation takes place.

Non-proportional loading effects have always presented challenges to the development of plasticity theory. The present micron-scale experiments reveal that the response of a square cross-sectioned cantilever beam subjected to bending about one axis followed by an abrupt transition to bending about an orthogonal axis is indeed non-trivial. There is a significant difference between the responses after the load transition between tests conducted maintaining constant force or constant displacement in the first loading direction. Both situations have been simulated. A significant strength elevation with decreasing cantilever size is evident in both stages of the bending response. One of the main concerns addressed in this paper is the non-proportional response immediately after the transition in the direction of bending, where the two competing versions of the single crystal SGP theories, incremental and non-incremental, generally predict distinctly different responses in the range when gradient effects are important. In fact, the comparison between the simulations and the experiments on the cantilever beams shows that, while the non-incremental version does predict a non-physical elastic gap immediately after the transition, that gap is small for the present loading configuration, especially for the case

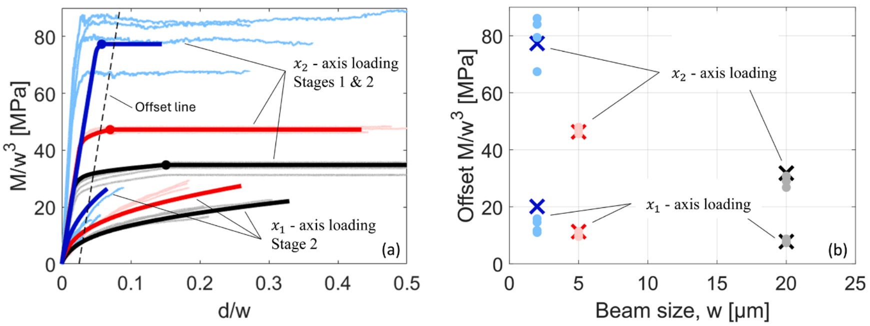

Fig. 13. Comparison of simulations and experimental measurements for sequential orthogonal bending of Cu <100> cantilever beams having square cross-sections of width $w = 2$, 5, and 20 μm. The Cu crystal axes are aligned with the Cartesian cantilever axes (x_i shown in Fig. 1), with x_3 parallel to the cantilever beam long axis. The transition from Stage 1 to Stage 2 in the relation between M_2/w^3 and d_2/w is indicated by a solid dot. In Stage 2, M_2 is held constant. (a) Scaled moment – displacement relations about the two bending axes from simulations (heavy lines) and experiments (light lines). (b) Simulated and experimentally measured scaled moments at the offset indicated in (a). The offset line has the same slope as the elastic response but shifted by 0.025. Colors distinguish cantilevers of different sizes: black for $w = 20$ μm, red for $w = 5$ μm, and blue for $w = 2$ μm.

where force or moment control is in effect in Stage 2. Over the loading histories carried out in the present experiments, the non-incremental version provides a reliable model of the elastic-plastic response, apart from the behavior immediately following the transition. This finding will be reassuring to researchers who employ the non-incremental model. Nevertheless, even if it is small, an elastic gap may have important consequences in some applications. An example is the plastic buckling of micron-scale columns or plates in compression. The non-incremental version predicts that plastic buckling of a micron-scale column subject to axial compression will not occur even when small deviations from straightness are included (Nielsen and Hutchinson, 2022). In the application to buckling, the elastic gap predicted by the theory at the onset of buckling results in a stiff elastic incremental bending stiffness which suppresses buckling. In contrast, buckling is predicted by the incremental version. To our knowledge, no micron-scale plastic column buckling experiments have been reported in the literature to date.

The absence of simulations for the 3D cantilever experiments based on the incremental single crystal SGP model will not have gone unnoticed by the reader. To our knowledge, no such code is available for 3D applications, or has ever been produced. Developing such a code for both versions of single crystal SGP was beyond the scope of this study. We hope that the present study has highlighted the potential importance of elastic-plastic behavior in the micron range and will motivate further development of robust 3D computational codes for accurate simulations. The capability of accurately modeling small-scale proportional and non-proportional loading scenarios will be impactful to a wide range of micro technology applications. (Fig. 13)

CRediT authorship contribution statement

Bin Zhang: Validation, Methodology, Investigation, Formal analysis, Data curation, Conceptualization. **Carl F.O. Dahlberg:** Writing – review & editing, Writing – original draft, Validation, Software, Methodology, Investigation, Formal analysis, Data curation, Conceptualization. **Tim Fischer:** Software, Methodology, Investigation, Formal analysis, Data curation. **J.W. Hutchinson:** Writing – review & editing, Writing – original draft, Validation, Software, Methodology, Investigation, Formal analysis, Data curation, Conceptualization. **W.J. Meng:** Writing – review & editing, Writing – original draft, Validation, Resources, Project administration, Methodology, Investigation, Funding acquisition, Formal analysis, Data curation, Conceptualization.

Declaration of competing interest

The authors declare that they have no known competing financial interests or personal relationships that could have appeared to influence the work reported in this paper.

Acknowledgements

B.Z. and W.J.M. acknowledge partial project support from the NSF EPSCoR program, under awards OIA-1946231 and OIA-2118756. Use of experimental facilities at the Louisiana State University Shared Instrumentation Facility (LSU SIF), a part of the Louisiana Core User Facilities (CUF), is acknowledged. W.J.M. acknowledges the generous support of Dr. B. Lu for the microplasticity research. C.F.O.D and T.F. acknowledge partial project support from the Center for Mechanics and Materials Design (MMD) at KTH.

Supplementary materials

Supplementary material associated with this article can be found, in the online version, at doi:10.1016/j.jmps.2025.106375.

Data availability

Data will be made available on request.

References

Abd-Elaziem, W., Elkatatny, S., Abd-Elaziem, A.E., Khedr, M., Abd El-baky, M.A., Hassan, M.A., Abu-Okail, M., Mohammed, M., Jarvenpaa, A., Allam, T., Hamada, A., 2022. On the current research progress of metallic materials fabricated by laser powder bed fusion process: a review. J. Mater. Res. Technol. 20, 681–707.

Aifantis, E.C., 1984. On the microstructural origin of certain inelastic models. Trans. ASME J. Eng. Mater. Technol. 106, 326–330.

Bardella, L., Niordson, C.F., 2020. Strain Gradient Plasticity: Theory and Implementation. In: Bertram, A., Forest, S. (Eds.), Mechanics of Strain Gradient Materials, CISM International Centre for Mechanical Sciences (Courses and Lectures), Mechanics of Strain Gradient Materials, CISM International Centre for Mechanical Sciences (Courses and Lectures), 600. Springer, pp. 101–149.

Benedetti, M., du Plessis, A., Ritchie, R.O., Dallago, M., Razavi, N., Berto, F., 2021. Architected cellular materials: a review on their mechanical properties towards fatigue-tolerant design and fabrication. Mater. Sci. Eng. R144, 100606/1–40.

Chen, K., Meng, W.J., Mei, F., Hiller, J., Miller, D.J., 2011. From micro- to nano-scale molding of metals: size effect during molding of single crystal Al with rectangular strip punches. Acta Mater. 59, 1112–1120.

Coleman, B.D., Noll, W., 1963. The thermodynamics of elastic materials with heat conduction and viscosity. Arch. Rational Mech. Anal. 13, 167–178.

Dahlberg, C.F.O., Boåsen, M., 2019. Evolution of the length scale in strain gradient plasticity. Int. J. Plast. 112, 220–241.

Dahlberg, C.F.O., Faleskog, J., 2013. An improved strain gradient plasticity formulation with energetic interfaces: theory and a fully implicit finite element formulation. Comput. Mech. 51, 641–659.

Dahlberg, C.F.O., Ortiz, M., 2020. Size scaling of plastic deformation in simple shear: Fractional strain-gradient plasticity and boundary effects in conventional strain-gradient plasticity. J. App. Mech. 87, 031017-1.

du Plessis, A., Razavi, N., Benedetti, M., Murchio, S., Leary, M., Watson, M., Bhate, D., Berto, F., 2022. Properties and applications of additively manufactured metallic cellular materials: a review. Prog. Mater. Sci. 125, 100918/1–43.

Fleck, N.A., Hutchinson, J.W., 1997. Strain gradient plasticity. Adv. Appl. Mech. 33, 295–361.

Fleck, N.A., Hutchinson, J.W., 2001. A reformulation of strain gradient plasticity. J. Mech. Phys. Solids. 49, 2245–2271.

Fleck, N.A., Willis, J.R., 2009. A mathematical basis for strain-gradient plasticity theory — Part I: scalar plastic multiplier &–Part II Tensorial plastic multiplier. J. Mech. Phys. Solids. 57, 1045–1057, 161–177 &.

Fleck, N.A., Muller, G.M., Ashby, M.F., Hutchinson, J.W., 1994. Strain gradient plasticity: theory and experiment. Acta Metall. Mater. 42 (2), 475–487.

Fleck, N.A., Hutchinson, J.W., Willis, J.R., 2014. Strain gradient plasticity under non-proportional loading. Proc. R. Soc. A 470, 20140267.

Fleck, N.A., Hutchinson, J.W., Willis, J.R., 2015. Guidelines for constructing strain gradient plasticity theories. J. Appl. Mech – Trans. ASME 82, 071002.

Geiger, M., Kleiner, M., Eckstein, R., Tiesler, N., Engel, U., 2001. Microforming. CIRP Annals - Manuf. Technol. 50 (2), 445–462.

Greer, J.R., De Hosson, J.T.M., 2011. Plasticity in small-sized metallic systems: Intrinsic versus extrinsic size effect. Prog. Mater. Sci. 56, 654–724.

Gudmundson, P., 2004. A unified treatment of strain gradient plasticity. J. Mech. Phys. Solids. 52, 1379–1406.

Gurtin, M.E., Anand, L., 2005. A theory of strain-gradient plasticity for isotropic, plastically irrotational materials — Part I: small deformations. J. Mech. Phys. Solids. 53, 1624–1649.

Gurtin, M.E., Anand, L., 2009. Thermodynamics applied to gradient theories involving the accumulated plastic strain: The theories of Aifantis and Fleck and Hutchinson and their generalization. J. Mech. Phys. Solids. 57, 405–421.

Gurtin, M.E., 2004. A gradient theory of small-deformation isotropic plasticity that accounts for the Burgers vector and for dissipation due to plastic spin. J. Mech. Phys. Solids. 52, 2545–2568.

Hill, R., 1966. Generalized constitutive relations for incremental deformation of metal crystals by multi-slip. J. Mech. Phys. Solids. 14, 95–102.

Hirth, J.P., Lothe, J., 1982. Theory of Dislocations, 2nd ed. Wiley, New York.

Hutchinson, J.W., 2012. Generalizing J2 flow theory: Fundamental issues in strain gradient plasticity. Acta Mechanica Sinica 28 (4), 1078–1086.

Jebahi, M., Cai, L., Abed-Meraim, F., 2020. Strain gradient crystal plasticity model based on generalized non-quadratic defect energy and uncoupled dissipation. Int. J. Plast. 126, 102617/1-24.

Krishna, A., Lee, J., 2018. Morphology-driven emissivity of microscale tree-like structures for radiative thermal management. Nanoscale Microscale Thermophys. Eng. 22 (2), 124–136.

Kuwabara, T., Van Bael, A., Iizuka, E., 2002. Measurement and analysis of yield locus and work hardening characteristics of steel sheets with different r-values. Acta Mater. 50, 3717–3729.

Liu, D., He, Y., Tang, X., Ding, H., Hu, P., Cao, P., 2012. Size effects in the torsion of microscale copper wires: Experiment and analysis. Scripta. Mater. 66, 406–409.

Liu, D., He, Y., Dunstan, D.J., Zhang, B., Gan, Z., Hu, P., Ding, H., 2013. Anomalous Plasticity in the Cyclic Torsion of Micron Scale Metallic Wires. Phys. Rev. Lett. 110, 244301/1–5.

Ma, Q., Clarke, D.R., 1995. Size dependent hardness of silver single crystals. J. Mater. Res. 10 (4), 853–863.

Malek, C.K., Saile, V., 2004. Applications of LIGA technology to precision manufacturing of high-aspect-ratio micro-components and -systems: a review. Microelectronics. J. 35 (2), 131–143.

Mei, F., Parida, P.R., Jiang, J., Meng, W.J., Ekkad, S.V., 2008. Fabrication, assembly, and testing of Cu- and Al-based microchannel heat exchangers. J. Microelectromechanical Syst. 17 (4), 869–881.

Motz, C., Weygand, D., Senger, J., Gumbsch, P., 2008. Micro-bending tests: A comparison between three-dimensional discrete dislocation dynamics simulations and experiments. Acta Mater. 56, 1942–1955.

Muhlhaus, H.B., Aifantis, E.C., 1991. A variational principle for gradient plasticity. Int. J. Solids. Struct. 28, 845–857.

Mukherjee, A., Banerjee, B., 2024. Elastic-gap free formulation in strain gradient plasticity theory. J. Appl. Mech. – Trans. ASME 91, 061008/1-13.

Nellemann, C., Niordson, C.F., Nielsen, K.L., 2017. An incremental flow theory for crystal plasticity incorporating gradient effects. Int. J. Solids. Struct. 110-111, 239–250.

Nielsen, K.L., Hutchinson, J.W., 2022. Plastic buckling of columns at the micron scale. Int. J. Solids. Struct. 257, 111558/1–10.

Panteghini, A., Bardella, L., Niordson, C.F., 2019. A potential for higher-order phenomenological strain gradient plasticity to predict reliable response under non-proportional loading. Proc. R. Soc. A 475, 20190258/1-21.

Peirce, D., Asaro, J., Needleman, A., 1983. Material rate dependence and localized deformation in crystalline solids. Acta Metall. 31 (12), 1951–1976.

Schürch, P., Osenberg, D., Testa, P., Bürki, G., Schwiedrzik, J., Michler, J., Koelmans, W.W., 2023. Direct 3D microprinting of highly conductive gold structures via localized electrodeposition. Mater. Des. 227, 111780/1–8.

Stolken, J.S., Evans, A.G., 1998. A microbend test method for measuring the plasticity length scale. Acta Mater. 46 (14), 5109–5115.

Uchic, M.D., Dimiduk, D.M., Florando, J.N., Nix, W.D., 2004. Sample dimensions influence strength and crystal plasticity. Science 1979 305, 986–989.

van Riel, M., van den Boogaard, A.H., 2007. Stress–strain responses for continuous orthogonal strain path changes with increasing sharpness. Scr. Mater. 57, 381–384.

Verma, R.K., Kuwabara, T., Chung, K., Haldar, A., 2011. Experimental evaluation and constitutive modeling of non-proportional deformation for asymmetric steels. Int. J. Plast. 27, 82–101.

Verma, P., Shekhar, C., Arya, S.K., Gopal, R., 2015. New design architecture of a 3-DOF vibratory gyroscope with robust drive operation mode and implementation. Microsyst. Technol. 21, 2175–2185.

Voyiadjis, G.Z., Song, Y., 2019. Strain gradient continuum plasticity theories: Theoretical, numerical and experimental investigations. Int. J. Plast. 121, 21–75.

Wang, Y., Cui, J., Li, Y., Zhang, Y., Zheng, S., Zhao, L., Hu, N., 2024. Deformation behavior and scale effects in microchannel hydroforming in ultra-thin TA1/CFRP fuel cell bipolar plates. Compos. Struct. 339, 118164/1–19.

Zhang, B., Song, Y., Voyiadjis, G.Z., Meng, W.J., 2018. Assessing texture development and mechanical response in microscale reverse extrusion of copper. J. Mater. Res. 33 (8), 978–988.

Zhang, B., Meng, A.C., Meng, W.J., 2021. Deviation of mechanical behavior in microforming from continuum scaling: a geometrically necessary dislocation storage perspective. Inter. J. Mach. Tools Manuf. 169, 103795/1–13.

Zhang, B., Nielsen, K.L., Hutchinson, J.W., Meng, W.J., 2023. Toward the development of plasticity theories for application to small-scale metal structures. PNAS 120 (44) e2312538120/1–12.